

A KERNEL-BASED LAGRANGIAN METHOD
FOR IMPERFECTLY-MIXED CHEMICAL
REACTIONS

by
Michael J. Schmidt

© Copyright by Michael J. Schmidt, 2018

All Rights Reserved

A thesis submitted to the Faculty and the Board of Trustees of the Colorado School of Mines in partial fulfillment of the requirements for the degree of Master of Science (Computational and Applied Mathematics).

Golden, Colorado

Date _____

Signed: _____
Michael J. Schmidt

Signed: _____
Dr. Stephen D. Pankavich
Thesis Advisor

Signed: _____
Dr. David A. Benson
Thesis Advisor

Golden, Colorado

Date _____

Signed: _____
Dr. Greg Fasshauer
Professor and Head
Department of Applied Mathematics and Statistics

ABSTRACT

Current Lagrangian (particle-tracking) algorithms used to simulate diffusion-reaction equations must employ a certain number of particles to properly emulate the system dynamics—particularly for imperfectly-mixed systems. The number of particles is tied to the statistics of the initial concentration fields of the system at hand. Systems with shorter-range correlation and/or smaller concentration variance require more particles, potentially limiting the computational feasibility of the method. For the well-known problem of bimolecular reaction, we show that using kernel-based, rather than Dirac delta, particles can significantly reduce the required number of particles. We derive the fixed half-width of a Gaussian kernel for a given reduced number of particles that analytically eliminates the error between kernel and Dirac solutions at any specified time. We also show how to solve for the fixed kernel size by minimizing the squared differences between solutions over any given time interval. Numerical results show that the half-width of the kernel should be kept below about 12% of the domain size, and that the analytic equations used to derive kernel size suffer significantly from the neglect of higher-order moments. The simulations with a kernel half-width given by least squares minimization perform better than those made to match at one specific time. A heuristic time-variable kernel size, based on the previous results, performs on par with the least squares fixed kernel size.

TABLE OF CONTENTS

ABSTRACT	iii
LIST OF FIGURES	vi
LIST OF SYMBOLS	vii
LIST OF ABBREVIATIONS	viii
ACKNOWLEDGMENTS	ix
CHAPTER 1 INTRODUCTION	1
CHAPTER 2 ANALYTIC MODEL AND METHODS	4
2.1 Governing equations	4
2.2 Exact solution for well-mixed system	4
2.3 Solution for a system with concentration fluctuations	5
2.4 Moment equations and initial conditions	6
CHAPTER 3 PARTICLE-TRACKING MODEL	8
3.1 Algorithm details	9
3.1.1 Convergence of algorithm to DRE	10
3.2 Determination of Gaussian kernel variance	10
3.2.1 Match at specific time	12
3.2.2 Least squares minimization	13
CHAPTER 4 PROPAGATION OF ERROR	14
CHAPTER 5 RESULTS	17
5.1 Specific time matching	18

5.2	Least squares matching	22
5.3	Variable kernel half-width matching	24
5.4	Comparison to Eulerian method	25
5.5	Domain effects	26
5.6	Slowdown in Gaussian particle reaction speed	27
CHAPTER 6 CONCLUSIONS		30
REFERENCES CITED		32
APPENDIX A INITIAL COVARIANCE RELATIONS FOR THE PARTICLE-TRACKING METHOD		35
APPENDIX B ESTIMATES FOR ERROR PROPAGATION		38

LIST OF FIGURES

Figure 5.1	Plots of particle-tracking simulations (symbols) and moment equation solutions (curves), using specific time matching for $t^* = 100$ ($t^*kC_0 = 500$), for a range of N_G/N_δ values.	18
Figure 5.2	Plots of particle-tracking simulations (symbols) and moment equation solutions (curves), using specific time matching for $t^* = 1000$ ($t^*kC_0 = 5000$), for a range of N_G/N_δ values. Arrows in (b) correspond to the plots shown in Figure 5.8(a)-(d).	19
Figure 5.3	Plots of particle-tracking simulations (symbols) and moment equation solutions (curves), using least squares matching for a range of N_G/N_δ values.	20
Figure 5.4	Plots of particle-tracking simulations (symbols) and moment equation solutions (curves), using variable ℓ_G matching for a range of N_G/N_δ values. Arrows in (b) correspond to the plots shown in Figure 5.8(a)-(b) and (e)-(f).	21
Figure 5.5	Plots of particle-tracking simulations and moment equation solutions as compared to an Eulerian finite difference solution, using the least squares matching criteria for $N_G/N_\delta = 0.1$ (corresponding to Figure 5.3(d)).	22
Figure 5.6	Plots of particle-tracking simulations (symbols) and moment equation solutions (curves), using specific time matching with $t^* = 1000$ ($t^*kC_0 = 5000$), $N_G/N_\delta = 0.1$ for a range of domain sizes.	23
Figure 5.7	Plots of numerical simulations (symbols) and moment equation solutions (curves), using variable ℓ_G matching with $N_G/N_\delta = 0.1$ for a range of domain sizes.	24
Figure 5.8	Plots of particle position/mass demonstrating moats phenomenon for Gaussian kernels (bottom two rows). Plots show $N_G/N_\delta = 0.5$ using: Dirac kernels, specific time matching (fixed ℓ_G) with $t^* = 1000$ ($t^*kC_0 = 5000$), and variable ℓ_G matching.	29

LIST OF SYMBOLS

Number of particles	N, N_i ($i = A, B$), N_p ($p = \delta, G$)
Number of spatial dimensions	d
Concentration [mol L^{-d}]	C, C_0, C_i ($i = A, B$), C_p ($p = \delta, G$)
Diffusion coefficient [$L^2 T^{-1}$]	D
Reaction rate constant [$L^d \text{ mol}^{-1} T^{-1}$]	k
Laplacian operator	$\Delta \equiv \nabla^2$
Real numbers	\mathbb{R}
Damköhler number	Da
Particle Damköhler number	\widehat{Da}
Ensemble-averaged concentration	\overline{C}
Zero-mean fluctuations in concentration	C'
Autocovariance of concentration fluctuations	$f(t, x, y) = \overline{C'_i(t, x)C'_i(t, y)}$, $i = A, B$
Cross-covariance of concentration fluctuations	$g(t, x, y) = \overline{C'_A(t, x)C'_B(t, y)}$
Mass of a particle	m, m_i ($i = A, B$), m_p ($p = \delta, G$)
Half-width of Gaussian kernel	ℓ_G
Size of d -dimensional domain	Ω
Time step length	Δt
Co-location probability of a particle pair separated by distance s , given Δt	$v(s; \Delta t)$
Spatial kernel of a particle	ϕ, ϕ_i ($i = A, B$), ϕ_p ($p = \delta, G$)
Expected value	\mathbb{E}

LIST OF ABBREVIATIONS

Diffusion-reaction equation	DRE
Reactive particle-tracking algorithm	RPT
Particle-number preserving/mass-based reactive particle-tracking algorithm	mRPT
Kernel-based reactive particle-tracking algorithm	kRPT
Moment equation	ME

ACKNOWLEDGMENTS

I would like to thank my advisors for their endless support, my committee for their valuable feedback, and my family for their love, patience, and support.

CHAPTER 1

INTRODUCTION

Chemical reactions can be simulated using several methods. In particular, the (well-mixed) thermodynamic governing equations can be approximated using classical grid-based Eulerian methods such as finite-differences or finite-elements. Below the scale of discretization—the subgrid scale—these techniques assume perfect mixing because at each node (or element, or cell), the concentration of each species is represented by a single, average number. The effects of the imperfect mixing of concentration fluctuations cannot be resolved at the subgrid level except by empirical adjustments to the thermodynamic reaction rates [e.g., 1–4]. Grid-based methods must also deal with the difficulties of the hyperbolic portion of transport when reacting fluids are in motion [e.g., 5–8].

A number of particle-based transport and reaction algorithms have been developed to deal with imperfect mixing and high-Péclet number flows. These particle reaction algorithms are largely extensions of the Gillespie algorithm [9, 10], with adjustments to handle spatial fluctuations of concentration in different ways. These include particle-on-lattice methods that share some of the subgrid averaging effects as the Eulerian methods and have been shown to exhibit further inaccuracies when the lattice is refined below some minimum size [11, 12]. A more accurate algorithm is gridless and calculates the exact probabilities of particle collision and reaction. The collisions are treated as independent [13] or biased by nearest-neighbor status [14]. Because collisions require a physically-based random motion, this method can be applied at any scale and under any type of diffusion [15]. However, particle methods are not without their limitations. If the reactions are simulated as a strict birth/death process, then the resolution for lower concentrations is limited to $\mathcal{O}(1/N)$, where N is the number of particles. This can be addressed by re-casting the birth/death process as a probabilistic, real-valued mass-reduction of individual particles [16]. Furthermore, reactions

that are more complex than bi-molecular seemingly require a calculation of the collision of multiple particles, which can be very time-consuming. This problem can be alleviated by placing multiple chemical species on each particle and limiting the particle collision process to mass exchange and local mixing [17].

One remaining problem with particle methods is that the initial particle number is not necessarily a modeling choice. *Paster et al.* [18] show that the required particle density in a finite domain is inversely proportional to the variance and the correlation length of a species' concentration fluctuations. In short, “smoother” fields defined by lower variance and short-range correlation require more particles—if they are treated as Dirac delta functions. Uniform (constant) initial concentrations would require an infinite number of particles, so clearly the method requires an alternative way to treat particles and their interaction. An interesting extension treats each particle as a kernel that possesses some mean position, mass, and shape, imparting some degree of smoothness to each particle [19]. It remains to be shown, however, how the particle number changes with the shape of the kernel, or more precisely: how closely can two simulations be made to match when one has a given number of Dirac particles and another has a smaller number of kernel-smoothed particles?

Thus, we intend to precisely address this question within the current text. First, in Chapter 2 we define an initial value problem for diffusion-driven bimolecular reactions that admits analytic solutions and has been numerically approximated by many methods [13, 16, 20]. We choose a problem that very clearly displays the reduced reaction rates engendered by imperfect mixing [21–23]. In Chapter 2 we also define the “match” between two different solutions. In Chapter 3 we define the numerical solutions for the Dirac and Gaussian kernel particles and identify the shape of the kernel based on user-defined particle numbers. In Chapter 4 we show that our approach and methods are well-founded by proving a quantitative bound on the error in our approximation methods. Finally, in Chapters 5 and 6 we show the results of ensembles of particle solutions and the approximate analytic equations for concentrations given Dirac versus Gaussian kernels of various size and provide some caveats

for kernel use.

CHAPTER 2
ANALYTIC MODEL AND METHODS

2.1 Governing equations

We consider a bimolecular reactive system where the transport of constituents is driven by diffusion. Two components in this system, A and B , react kinetically and irreversibly with one another such that $A + B \rightarrow \emptyset$. For an infinite, d -dimensional space, the governing equation for transport of the components is the diffusion-reaction equation (DRE)

$$\frac{\partial C_i}{\partial t} - D\Delta C_i = -kC_A C_B, \quad i = A, B, \quad x \in \mathbb{R}^d, \quad t > 0, \quad (2.1)$$

where the concentration of species i is given by $C_i = C_i(t, x)$ [mol L^{-d}], D is the diffusion coefficient [L² T⁻¹], and k [L^d mol⁻¹ T⁻¹] is the reaction rate constant. The reaction rate $r = kC_A C_B$ is assumed to be given by the law of mass action. If C_0 is the initial mean concentration of both A and B particles, this system can be characterized using a single dimensionless quantity, known as the Damköhler number, $Da := kC_0 a^2 / D$, where a is some characteristic length-scale of diffusive mixing, typically given by the concentration autocorrelation length.

2.2 Exact solution for well-mixed system

When the system is well-mixed in space at all times, concentrations are spatially homogeneous (i.e., constant in x), and the diffusion term in (2.1) can be dropped. For this case, called the thermodynamic limit, well-known analytical solutions exist. For the simplest case, in which the initial average concentrations are equal $C_A(0, x) = C_B(0, x) = C_0 > 0$, Equation (2.1) becomes $\frac{dC_i}{dt} = -kC_i^2$, and the exact solution is merely

$$C_i(t) = \frac{C_0}{1 + C_0 k t}, \quad (2.2)$$

which tends to zero like t^{-1} for large time.

2.3 Solution for a system with concentration fluctuations

Keeping the thermodynamic limit in mind, we are interested in the more complex case where concentrations have some random initial distribution, and the system is not continuously well-mixed. For this setup, concentrations evolve by diffusion as described by the DRE (2.1). We may decompose concentrations into mean and fluctuation terms, such that

$$C_i(t, x) = \overline{C}_i(t) + C'_i(t, x), \quad (2.3)$$

where the overbar refers to the ensemble average and the prime to the zero-mean fluctuations about the average. We assume the system is ergodic, such that the ensemble average and spatial average are interchangeable, and only depend on t . Restrictions associated with the assumption of ergodicity are discussed, for example, by *Tartakovsky et al.* [24]. Broadly speaking, the larger the physical domain, the better the assumption of ergodicity, as larger domains can allow for a full ensemble of statistics. We shall also assume that the initial concentration distributions of species A and B have identical spatial autocovariance at $t = 0$. These assumptions allow one to obtain an analytical solution for the problem but are not required for numerical simulations. With these assumptions, the spatial averages of the initial concentrations of A and B are equal, i.e.,

$$\overline{C}_A(0, x) = \overline{C}_B(0, x) \equiv C_0, \quad (2.4)$$

and clearly, due to the 1:1 stoichiometric ratio of the reaction, their average concentrations are equal for all $t \geq 0$, i.e.,

$$\overline{C}_A(t) = \overline{C}_B(t) = \overline{C}(t). \quad (2.5)$$

Substituting (2.3) into (2.1) and taking the ensemble average of the equation, we obtain an equation for the average concentration, namely

$$\frac{d\overline{C}}{dt} = -k \left(\overline{C}^2 + \overline{C'_A C'_B} \right), \quad (2.6)$$

where the last term, $\overline{C'_A(t, x)C'_B(t, x)}$, is the cross-covariance between concentration deviations. For a highly-mixed system, this term is negligible compared to the other terms in the

equation, but this is no longer the case when species segregation occurs. During segregation, A and B typically develop anti-correlation properties, so this term becomes negative, slowing the mean reaction rate. Ultimately, we want to solve for the average concentration \bar{C} , but to do this we must first derive an explicit expression for the cross-covariance. With this in mind, we subtract the equation for the mean concentration (2.6) from (2.1) to obtain an evolution equation for the concentration deviation

$$\frac{\partial C'_i}{\partial t} - D\Delta C'_i = -k\bar{C}(C'_A + C'_B) - kC'_A C'_B + k\overline{C'_A C'_B}, \quad i = A, B. \quad (2.7)$$

2.4 Moment equations and initial conditions

Equations for the evolution of the autocovariance $f(t, x, y) = \overline{C'_i(t, x)C'_i(t, y)}$, $i = A, B$, and the cross-covariance $g(t, x, y) = \overline{C'_A(t, x)C'_B(t, y)}$ can be obtained from (2.7). Details of the derivation are given in *Paster et al.* [18]. The resulting moment equations are

$$\begin{aligned} \frac{\partial f}{\partial t} - 2D\Delta f &= -2k [\bar{C}(t)(f + g) + h_1(t, x, y)], \\ \frac{\partial g}{\partial t} - 2D\Delta g &= -2k [\bar{C}(t)(f + g) + h_1(t, x, y)], \end{aligned} \quad (2.8)$$

where $h_1(t, x, y) = \overline{C'_A(t, x)C'_B(t, x)C'_A(t, y)}$ is a third order moment. Taking the sum and difference of the moment equations yields two independent equations for $f + g$ and $f - g$, respectively. These are

$$\begin{aligned} \frac{\partial}{\partial t}(f + g) - 2D\Delta(f + g) &= -4k [\bar{C}(t)(f + g) + h_1(t, x, y)], \\ \frac{\partial}{\partial t}(f - g) - 2D\Delta(f - g) &= 0. \end{aligned} \quad (2.9)$$

Assuming that $|\bar{C}(t)(f + g)| \gg |h_1|$, we can neglect the third order moment and arrive at an approximate solution to the system of PDEs. We shall return to this assumption in Chapter 5 by using results from numerical simulations to examine its validity.

Various initial conditions could be assumed for f and g . Since we are ultimately interested in showing the correlation between numerical particle models and the analytical solutions of the system, we will focus on synthetic initial conditions that match those imposed in the numerical simulations, given Dirac delta or Gaussian kernel representations (see Appendix

A). For simplicity and to match numerical results, we assume that the initial cross-covariance is identically zero for each of the different systems (denoted by subscript), namely

$$g_\delta(0, x, y) = g_G(0, x, y) \equiv 0,$$

whereas the autocovariance for the Dirac delta particles is

$$f_\delta(0, x, y) = C_0 m_\delta \left[\delta(x - y) - \frac{1}{\Omega} \right], \quad (2.10)$$

and for the Gaussian particles is

$$f_G(0, x, y) = C_0 m_G \left[\frac{1}{(4\pi\ell_G^2)^{d/2}} e^{-\frac{|x-y|^2}{4\ell_G^2}} - \frac{1}{\Omega} \right], \quad (2.11)$$

where m_δ and m_G are the mass of single Dirac or Gaussian particle, respectively, ℓ_G is the half-width of a Gaussian kernel, and Ω is the size of a d -dimensional domain in a corresponding particle-tracking simulation (Appendix A).

For these initial conditions and neglecting the effects of higher-order moments like h_1 , the solution of (2.9) gives rise to a time-dependent cross-correlation function for particle types $p = \delta, G$ (see *Paster et al.* [18], Appendices A and B for details regarding this derivation):

$$g_p(t) = \frac{1}{2(8\pi Dt)^{d/2}} \int f_p(0, z, x) e^{-\frac{|x-z|^2}{8Dt}} dz \left[-1 + \exp \left(-4k \int_0^t \overline{C}_p(\tau) d\tau \right) \right]. \quad (2.12)$$

We note that if $f_p(0, z, x)$ is a function of $|x - z|$ only (as in (2.10) and (2.11)), then g_p is independent of x , and thus, we write $g_p(t)$ instead of $g_p(t, x, x)$. Finally, (2.12) can be substituted into (2.6) to obtain a closed-form, integro-differential equation for the mean concentration

$$\frac{d\overline{C}_p}{dt} = -k\overline{C}_p^2 - \frac{k}{2(8\pi Dt)^{d/2}} \int f_p(0, z, x) e^{-\frac{|x-z|^2}{8Dt}} dz \left[-1 + \exp \left(-4k \int_0^t \overline{C}_p(\tau) d\tau \right) \right], \quad (2.13)$$

subject to the initial condition $\overline{C}_p(0) = C_0$, with $p = \delta, G$. An explicit representation for the solution of this equation cannot be obtained, but the equation can be solved numerically.

CHAPTER 3

PARTICLE-TRACKING MODEL

Benson and Meerschaert [13] developed their reactive particle-tracking (RPT) algorithm in order to stochastically simulate the DRE using a large number of point-particles (numerically-represented by Dirac deltas). *Paster et al.* [18] showed that the initial number of particles necessary for accurate simulation is based on the initial auto- and cross-covariance structure of the system of interest. These authors also show that for systems with either high concentration variance or high correlation of concentration fluctuations, RPT simulations require a relatively small number of particles, while in short-range, low variance systems, the number of particles required to capture this behavior tends toward infinity, making simulations computationally infeasible.

The RPT algorithm uses a particle-killing approach, wherein particles are eliminated from the system after reaction. However, *Bolster et al.* [16] discuss a particle-number conserving, mass-based version of RPT (mRPT), in which all particles are given an initial mass that is reduced based on its probability of reaction with every particle of opposite species in the domain. As a result, mRPT is able to depict concentrations of reactant with a higher level of resolution but still requires a uniquely-determined number of point-particles, informed by the initial conditions.

This text outlines a kernel-based RPT (kRPT) method, which allows the user to reduce the number of particles in a given simulation while still achieving similar results. This is done by “smearing” the mass of the point particles in mRPT using a kernel representation (Gaussian kernels are used for computational convenience) and thereby smoothing the concentration profile that was coarsened by the decrease in particle number. However, of particular concern is the level of smoothing desired (determined by the half-width of the Gaussian kernel), as an inappropriate choice of kernel size will lead to over- or underpredic-

tion of the rate of reaction. The method for determining kernel size, based on the desired number of particles, is discussed in detail within Section 3.2.

3.1 Algorithm details

The kRPT algorithm initializes the domain by assigning initial particle positions according to draws from a uniform distribution. Diffusion and reaction are simulated separately by operator splitting within each time step, and, without loss of generality, we will assume reactions are calculated first. Reactions are calculated according to the mRPT algorithm of *Bolster et al.* [16] (with the significant difference lying in the increased co-location probability for Gaussian particles, due to the kernel’s increased spatial spread). Reactions are performed for each time step by reduction in mass and determined probabilistically, based on separation distance, according to the following algorithm (without loss of generality, as to the choice of inner and outer loop)

$$\begin{aligned}
 &\mathbf{for} \ j = 1 : N_A \\
 &\quad \mathbf{for} \ l = 1 : N_B \\
 &\quad\quad \Delta m_{j,l} = k \Delta t \ m_{A,j} m_{B,l} \ v(x_{A,j} - x_{B,l}; \Delta t) \\
 &\quad\quad m_{A,j} = m_{A,j} - \Delta m_{j,l} \quad , \\
 &\quad\quad m_{B,l} = m_{B,l} - \Delta m_{j,l} \\
 &\quad \mathbf{end} \\
 &\mathbf{end}
 \end{aligned} \tag{3.1}$$

such that

$$\begin{aligned}
 m_{A,j}(t + \Delta t) &= m_{A,j}(t) - \sum_{l=1}^{N_B} \Delta m_{j,l}(t), \\
 m_{B,l}(t + \Delta t) &= m_{B,l}(t) - \sum_{j=1}^{N_A} \Delta m_{j,l}(t),
 \end{aligned} \tag{3.2}$$

where $m_{A,j}$, $m_{B,l}$ and $x_{A,j}$, $x_{B,l}$ are the masses and positions of the j^{th} and l^{th} particle of A and B reactants, respectively, $\Delta m_{j,l}$ is the mass reduction due to reaction between the j^{th} and l^{th} particle pair, N_i is the number of particles ($i = A, B$), D is assumed to be the same for A and B , Δt is the constant length of a time step, and $v(s; \Delta t)$ represents the co-location probability of an individual A and B particle pair, based on their separation distance s ,

given the parameter Δt . This co-location probability is calculated as follows

$$v(s; \Delta t) = \frac{1}{[4\pi (\ell_G^2 + 2D\Delta t)]^{d/2}} \exp \left[-\frac{|s|^2}{4 (\ell_G^2 + 2D\Delta t)} \right], \quad (3.3)$$

where ℓ_G is the half-width of the Gaussian kernel and $2D\Delta t$ is the variance of the diffusion kernel, based on Brownian motion. The positions $x_{A,j}$ and $x_{B,l}$ evolve according to the stochastic Langevin equation

$$x_n(t + \Delta t) = x_n(t) + \xi_n \sqrt{2D\Delta t}, \quad (3.4)$$

where x_n is a vector of particle locations, and ξ_n is a vector of independent standard Normal variables, as derived from Fick's Law.

3.1.1 Convergence of algorithm to DRE

In order to ensure that the kRPT algorithm is valid for solving diffusion-reaction problems, it would be desirable to show that it converges to the underlying DRE as $\Delta t \rightarrow 0$. *Paster et al.* [25] demonstrate this convergence for the particle-killing method (RPT) that is the predecessor of mRPT. Additionally, *Bolster et al.* [16] show a similar proof for the mRPT algorithm that is the Dirac particle analog of kRPT. Considering the proof of *Bolster et al.*, it is clear that the proof in the kRPT case follows similarly for any non-Dirac kernel that is (a) a valid density (i.e., the kernel is nonnegative and integrates to unity), and (b) both radially-symmetric and even with respect to the origin in the radial variable. As a result, using the proposed kernels with co-location probability $v(s)$, given by (3.3), would result in the kRPT algorithm converging to the DRE as the defined time step, Δt , tends to zero.

3.2 Determination of Gaussian kernel variance

As defined in Appendix A, Gaussian particles will be represented in space by the following kernel

$$\phi_G(x - y) = \frac{1}{(2\pi\ell_G^2)^{d/2}} e^{-\frac{|x-y|^2}{2\ell_G^2}}, \quad (3.5)$$

where ϕ_G is a radially-symmetric Gaussian (i.e., half-width is equal in each direction).

Initial concentrations in the system are fixed, and thus the total mass is as well with $C_0 = m_{total}/\Omega$, and $m_{total} = m_p N_p$, where m_p is the mass of a single particle of N_p total particles ($p = \delta, G$). This means that once the desired number of particles in the Gaussian simulation (N_G) is chosen, then m_G is determined. In order to solve for ℓ_G in (3.5), the Gaussian kernel's half-width, we turn to the underlying equation for $\overline{C}(t)$ given in (2.13)

$$\frac{d\overline{C}_p}{dt} = -k \left(\overline{C}_p^2 + g_p(t) \right). \quad (3.6)$$

Equation (3.6) is subject to the following initial conditions, which should match the starting conditions of the particle methods. Thus, we define the initial conditions, $f_\delta(0, x, y)$ and $f_G(0, x, y)$, to be equal to $\widehat{f}_\delta(0, x, y)$ and $\widehat{f}_G(0, x, y)$, the autocovariance functions for the particle simulations, as derived in Appendix A:

$$\begin{aligned} f_\delta(0, x, y) &:= \sigma_\delta^2 \ell_\delta^d \left[\delta(x - y) - \frac{1}{\Omega} \right] \\ &= \frac{C_0^2 \Omega}{N_\delta} \left[\delta(x - y) - \frac{1}{\Omega} \right] \\ &= C_0 m_\delta \left[\delta(x - y) - \frac{1}{\Omega} \right] = \widehat{f}_\delta(0, x, y), \\ f_G(0, x, y) &:= C_0 m_G \left[\frac{1}{(4\pi \ell_G^2)^{d/2}} e^{-\frac{|x-y|^2}{4\ell_G^2}} - \frac{1}{\Omega} \right] = \widehat{f}_G(0, x, y), \\ g_p(0, x, y) &:\equiv 0, \quad p = \delta, G, \end{aligned} \quad (3.7)$$

because as established by *Paster et al.* [18], $\sigma_\delta^2 \ell_\delta^d = C_0^2 \Omega / N_\delta$. Naïvely, one might attempt to match a Gaussian simulation to a corresponding Dirac simulation by matching properties of the autocovariance functions, f_δ and f_G in (3.7). However, this would imply $m_G = m_\delta$ and $\ell_G = 0$, turning the Gaussian into a Dirac delta, and making the result trivial. This implies a more nuanced approach is necessary.

We will show in Chapter 4 that the error in $\overline{C}_G(t)$ for differing kernel choices is almost entirely determined by the quantity $\epsilon := |g_\delta(t) - g_G(t)|$ (see Equation (4.6)). With the goal of minimizing this quantity, we substitute the initial autocovariance choices from (3.7) into (2.12) and arrive at the following equations for the cross-covariance functions

$$\begin{aligned}
g_\delta(t) &= \frac{C_0 m_\delta \left(e^{-4k \int_0^t \bar{C}_\delta(\tau) d\tau} - 1 \right)}{2} \left[\frac{1}{(8\pi Dt)^{d/2}} - \frac{1}{\Omega} \right], \\
g_G(t) &= \frac{C_0 m_G \left(e^{-4k \int_0^t \bar{C}_G(\tau) d\tau} - 1 \right)}{2} \left[\frac{1}{[4\pi (\ell_G^2 + 2Dt)]^{d/2}} - \frac{1}{\Omega} \right].
\end{aligned} \tag{3.8}$$

Using fixed parameters of the simulation, and our choice of N_G , we may choose ℓ_G such that ϵ is minimized. Here, we propose two methods for minimizing ϵ .

3.2.1 Match at specific time

The most straightforward way of minimizing ϵ is choosing a particular time, t^* , at which the user would like the simulations to “match,” so that $g_G(t^*) = g_\delta(t^*)$, which implies $\epsilon(t^*) = 0$. We assume here that $|\bar{C}_\delta - \bar{C}_G| \approx 0$ on the interval $[0, t^*]$, a claim supported by Equation (4.7). This allows us to cancel the exponential terms in g_δ and g_G and solve for ℓ_G using only the parameters of the system. Thus, we may attain a value for $\ell_G(t^*)$ by setting $g_\delta(t^*) = g_G(t^*)$ in (3.8) and solving, which gives

$$\ell_G(t^*) = \sqrt{\frac{1}{4\pi} \left[\frac{N_G}{N_\delta} \left[(8\pi Dt^*)^{-d/2} - \frac{1}{\Omega} \right] + \frac{1}{\Omega} \right]^{-2/d} - 2Dt^*}. \tag{3.9}$$

Here, we note that the form of (3.9) implies that, for given parameters, there is some maximum value of t^* , which we will call τ^* , such that

$$\tau^* := \max \left\{ t^* : \left[\frac{N_G}{N_\delta} \left[(8\pi Dt^*)^{-d/2} - \frac{1}{\Omega} \right] + \frac{1}{\Omega} \right]^{-2/d} - 8\pi Dt^* \geq 0 \right\}, \tag{3.10}$$

and after which, values for ℓ_G will become imaginary, and hence, non-physical. However, the value of τ^* is highly sensitive to the parameters D and Ω , simply implying that certain choices of t^* may not be appropriate for systems with particular Damköhler numbers. Note, also, that the left side of the inequality in (3.10) is equal to zero only when $N_G = N_\delta$ and greater than zero when $N_G < N_\delta$.

This method of minimization will produce a result in which Dirac- and Gaussian-based moment equation solutions will match at or near t^* and allows the user to decide when the differing simulations will display similar behavior.

3.2.2 Least squares minimization

Alternatively, the user may define a set of times, $T^* = \{t_0, t_1, \dots, t_n\}$, over which the quantity

$$\epsilon(\ell_G) := \left(\sum_{k=1}^n |\bar{C}_\delta(t_k) - \bar{C}_G(t_k; \ell_G)|^2 \right)^{1/2}, \quad (3.11)$$

may be minimized to determine

$$\ell_G^* := \operatorname{argmin}_{\ell_G \in (0, \frac{1}{c}\Omega]} \epsilon(\ell_G), \quad (3.12)$$

where the upper-bound for the value of ℓ_G is some fraction of the domain, Ω . This will produce a single corresponding value for $\ell_G = \ell_G^*$, which will minimize the overall error between Dirac- and Gaussian-based moment equation solutions, subject to the chosen set of times T^* .

CHAPTER 4
PROPAGATION OF ERROR

In considering the differing initial autocovariances arising from Dirac versus Gaussian kernels, as shown in (3.7), one arrives at two different solutions of the diffusion-reaction equation for $g(t)$. In either case, the form of g is the same, namely

$$g_p(t) = \psi_p(t) \left[-1 + \exp \left(-4k \int_0^t \overline{C}_p(\tau) d\tau \right) \right], \quad (4.1)$$

where

$$\psi_p(t) := \frac{1}{2(8\pi Dt)^{d/2}} \int f_p(0, z, x) e^{-\frac{|x-z|^2}{8Dt}} dz, \quad (4.2)$$

for $p = \delta, G$. We note that ψ does not depend upon x because each of the initial conditions (2.10)-(2.11) is a function only of the difference $x - y$, rather than x and y independently, and the integral is translation invariant. In particular, a few brief calculations show that

$$\psi_\delta(t) = \frac{1}{2} C_0 m_\delta \left[\frac{1}{(8\pi Dt)^{d/2}} - \frac{1}{\Omega} \right], \quad (4.3)$$

and

$$\psi_G(t) = \frac{1}{2} C_0 m_G \left[\frac{1}{(4\pi(\ell_G^2 + 2Dt))^{d/2}} - \frac{1}{\Omega} \right]. \quad (4.4)$$

For each g_p , we have a corresponding mean concentration $\overline{C}_p(t)$ defined as the solution of the initial-value problem

$$\left. \begin{aligned} \frac{d\overline{C}_p}{dt} &= -k \left[\overline{C}_p^2 + g_p(t) \right] \\ \overline{C}_p(0) &= C_0 \end{aligned} \right\}. \quad (4.5)$$

Thus, in order to estimate the error in the resulting mean concentration stemming from the use of a different (and non-Dirac delta) autocorrelation function, we first assume, without loss of generality, that $\overline{C}_G(t) \geq \overline{C}_\delta(t)$. Therefore, to estimate the difference in these quantities, we subtract (4.5) in the case $p = \delta$ from (4.5) in the case $p = G$ so that

$$\begin{aligned}
\frac{d}{dt} (\bar{C}_G - \bar{C}_\delta) &= -k (\bar{C}_G^2 - \bar{C}_\delta^2) - k(g_G - g_\delta) \\
&= -k(\bar{C}_G + \bar{C}_\delta)(\bar{C}_G - \bar{C}_\delta) + k(g_\delta - g_G).
\end{aligned}$$

Using the lower bound for each mean concentration, (B.3), in Appendix B, this becomes

$$\frac{d}{dt} (\bar{C}_G - \bar{C}_\delta) \leq -\frac{2kC_0}{1 + kC_0t} (\bar{C}_G - \bar{C}_\delta) + k(g_\delta - g_G).$$

Now, using the integrating factor $p(t) = (1 + kC_0t)^2$, we can rearrange the inequality and integrate using $\bar{C}_\delta(0) = \bar{C}_G(0) = C_0$ to find

$$\bar{C}_G(t) - \bar{C}_\delta(t) \leq \frac{k}{(1 + kC_0t)^2} \int_0^t [g_\delta(\tau) - g_G(\tau)] (1 + kC_0\tau)^2 d\tau.$$

Since these same computations can be repeated on intervals of time in which $\bar{C}_\delta(t) \geq \bar{C}_G(t)$ we combine them with absolute values, resulting in

$$|\bar{C}_G(t) - \bar{C}_\delta(t)| \leq \frac{k}{(1 + kC_0t)^2} \int_0^t |g_\delta(\tau) - g_G(\tau)| (1 + kC_0\tau)^2 d\tau. \quad (4.6)$$

Thus, the difference in mean concentration can be estimated in terms of $|g_\delta(\tau) - g_G(\tau)|$ only.

Next, we need to estimate the difference in the cross-correlation functions caused by the differing initial autocorrelation structure. This is performed in detail within Appendix B, resulting in (B.5), namely

$$|g_\delta(t) - g_G(t)| \leq \frac{1}{2} C_0^2 \Delta + \frac{C_0^2 \Delta}{2\Omega(1 + kC_0t)^{d/2}} + \frac{\pi d C_0 \ell_G^2 m_G}{(1 + kC_0t)^{1+d/2}} + \frac{C_0 m_\delta}{2\Omega(1 + kC_0t)^4},$$

where

$$\Delta := \frac{1}{N_G} - \frac{1}{N_\delta} = \frac{1}{N_G} \left(1 - \frac{N_G}{N_\delta} \right)$$

can be chosen as small as one wishes. Inserting this expression for the difference in cross-correlations into (4.6), we find

$$\begin{aligned}
|\bar{C}_G(t) - \bar{C}_\delta(t)| &\leq \frac{k}{(1 + kC_0t)^2} \int_0^t \left[(1 + kC_0\tau)^2 \frac{1}{2} C_0^2 \Delta + \frac{C_0^2 \Delta}{2\Omega(1 + kC_0\tau)^{d/2-2}} \right. \\
&\quad \left. + \frac{\pi d C_0 \ell_G^2 m_G}{(1 + kC_0\tau)^{-1+d/2}} + \frac{C_0 m_\delta}{2\Omega(1 + kC_0\tau)^2} \right] d\tau \\
&\leq \frac{1}{(1 + kC_0t)^2} [C_1 \Delta (1 + kC_0t)^3 + C_2 \Delta (1 + kC_0t)^{3-d/2} \\
&\quad + C_3 (1 + kC_0t)^{2-d/2} + C_4] \\
&= C_1 \Delta (1 + kC_0t) + C_2 \Delta (1 + kC_0t)^{1-d/2} \\
&\quad + C_3 (1 + kC_0t)^{-d/2} + C_4 (1 + kC_0t)^{-2},
\end{aligned}$$

where C_1, C_2, C_3 , and C_4 are constants defined by the terms within the first and second lines above. For t large, the second, third, and fourth terms are negligible compared to the first. Hence, denoting the stopping time of a simulation by T , the difference in the mean concentration computed by the RPT method and the kRPT implementation satisfies

$$|\bar{C}_G(t) - \bar{C}_\delta(t)| \leq C_1 \Delta (1 + kC_0T). \quad (4.7)$$

Of course, choosing Δ sufficiently small will allow for as great an order of accuracy as one wishes. In particular, if one chooses $\Delta = 0$, which occurs when $N_G = N_\delta$, the error instead satisfies

$$|\bar{C}_G(t) - \bar{C}_\delta(t)| \leq C_3 (1 + kC_0T)^{-d/2}, \quad (4.8)$$

which actually decreases with T , and this error is incurred due only to the difference in initial covariance structure.

CHAPTER 5

RESULTS

Numerical simulations were conducted in MATLAB, using a MacBook Pro with a 2.9 GHz Intel Core i5 processor and 8 GB of RAM. All simulations were conducted for $d = 1$ spatial dimensions, and six-realization ensembles were employed in order to average the stochastic variability of particle-tracking simulations. In all plots showing domain-averaged concentration versus time, the well-mixed analytical solution (2.2) is shown as a solid black line for reference, moment equation (ME) solutions (2.13) are shown as solid curves, and particle-tracking solutions are shown as diamond-shaped scatter plots with error bars corresponding to ± 1 standard deviation among realizations in the ensemble. As well, red plots (solid curve, empty diamonds) represent Dirac kernel simulations, and blue plots (dashed curve, filled diamonds) represent Gaussian kernel simulations. The domain size for all initial cases is $\Omega = 1$ and is expanded when considering domain effects.

In this chapter, we characterize the simulations by their particle Damköhler number, as defined in *Bolster et al.* [16], $\widehat{Da} := kC_0\Delta x^2/D$, where Δx , the average inter-particle spacing ($\Delta x = \Omega/N_p$, $p = \delta, G$), is used as the characteristic length-scale of diffusive mixing. Note that this characterization of the system is derived using Dirac particles, and, for all numerical simulations in this chapter, $\widehat{Da} = 0.5$ will describe the Dirac particle base cases ($D = 1.0 \times 10^{-5}$, $k = 5.0$, $C_0 = 1.0$).

Throughout this chapter, we will show the results of numerical simulations for $N_G = \{900, 500, 300, 100\}$ and compare them to the base case of $N_\delta = 1000$. Solution matching criteria used will be: specific time matching for $t^* = \{100, 1000\}$, least squares matching, and a heuristically-motivated variable kernel half-width matching. Additionally, the various influences of the ratio of kernel half-width to domain size (ℓ_G/Ω) will be examined for several sub-cases.

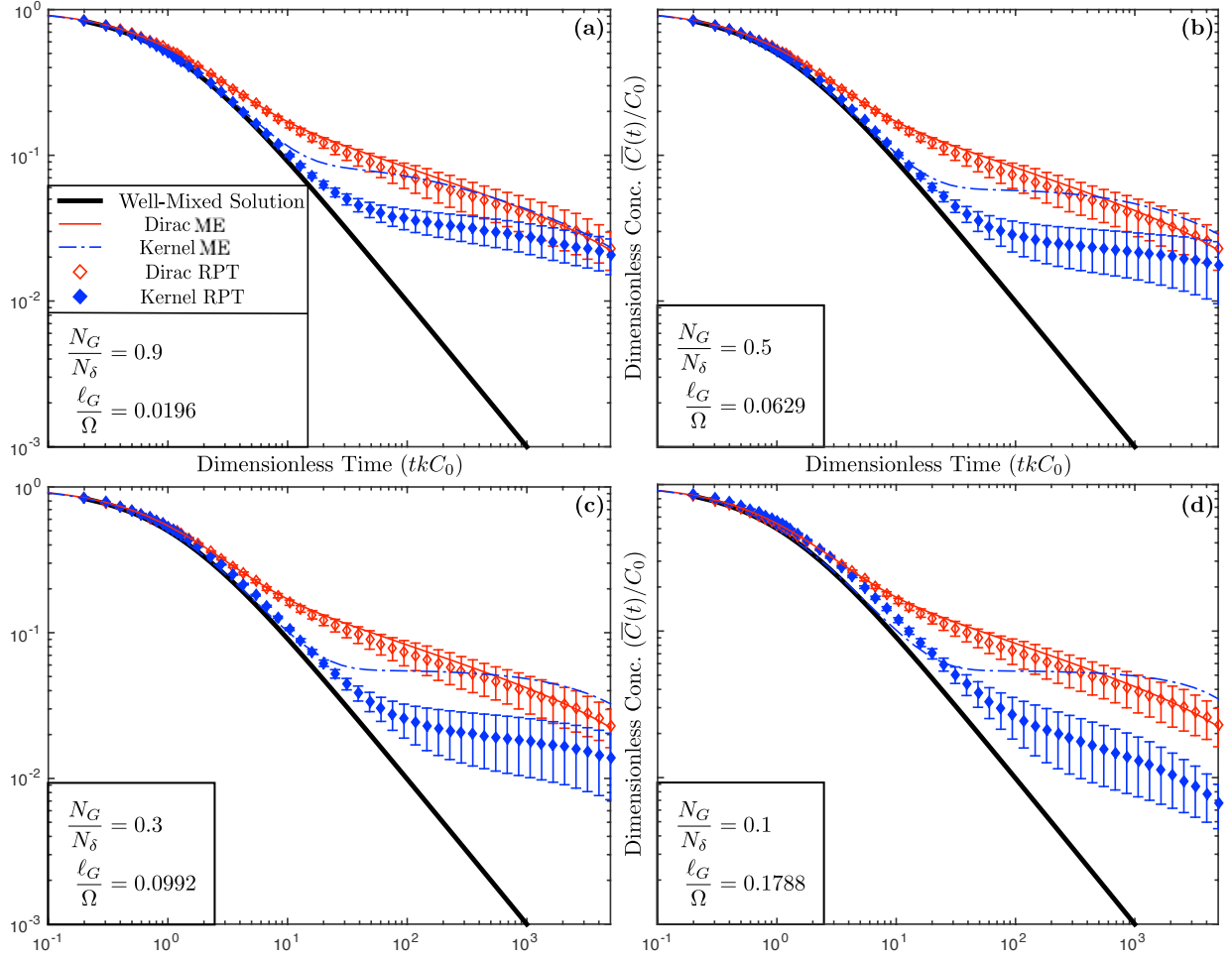


Figure 5.1: Plots of particle-tracking simulations (symbols) and moment equation solutions (curves), using specific time matching for $t^* = 100$ ($t^*kC_0 = 500$), for a range of N_G/N_δ values.

5.1 Specific time matching

As the simplest and most straightforward approach to matching Dirac and Gaussian particle-tracking solutions, we first use the specific time matching criteria put forth in Section 3.2.1. Simulations were run for $t^* = \{100, 1000\}$. As depicted in Figure 5.1(a) and Figure 5.2(a), we predictably see very close agreement between the particle-tracking and moment equation solutions for $N_G/N_\delta = 0.9$. As well, in both cases, the Dirac and Gaussian particle-tracking solutions become “close” near t^* (the error in dimensionless concentration

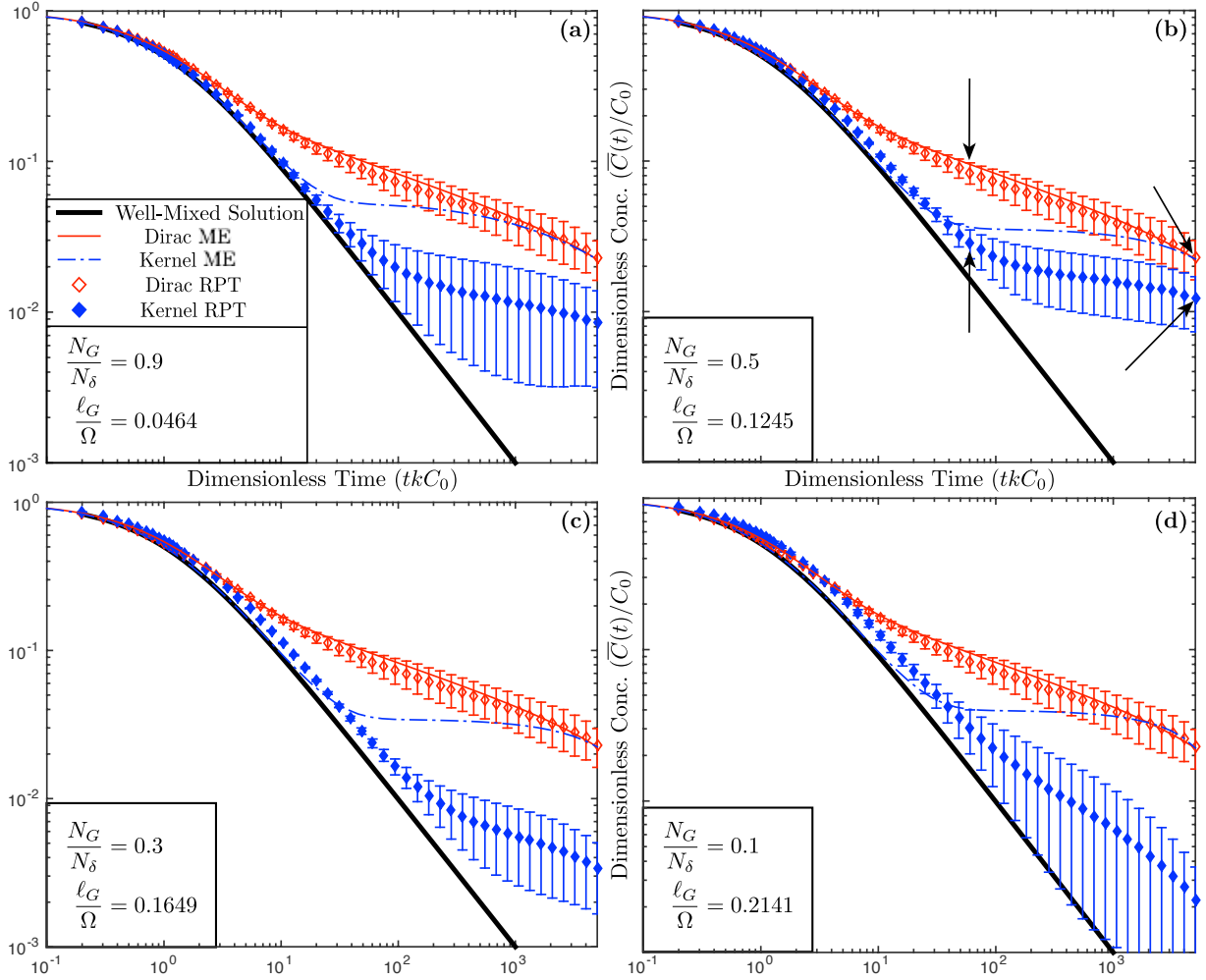


Figure 5.2: Plots of particle-tracking simulations (symbols) and moment equation solutions (curves), using specific time matching for $t^* = 1000$ ($t^*kC_0 = 5000$), for a range of N_G/N_δ values. Arrows in (b) correspond to the plots shown in Figure 5.8(a)-(d).

between the Dirac and particle-tracking solutions at t^* is $\mathcal{O}(1/100)$, or approximately the initial mass of 10 Gaussian particles), and remain close thereafter in the $t^* = 100$ case. However, one does notice the overprediction of concentration by the moment equation solutions (blue curves), versus the particle-tracking solutions for the Gaussian kernels. In the cases of $N_G/N_\delta = 0.9$ (Figure 5.1(a) and Figure 5.2(a)), we attribute this to the neglect of third-order moments in the moment equation paradigm, as mentioned in Section 2.4. These third-order moments appear to become more significant as N_G decreases (and ℓ_G increases), causing an increasing discrepancy between moment equation and particle-tracking solutions as N_G/N_δ

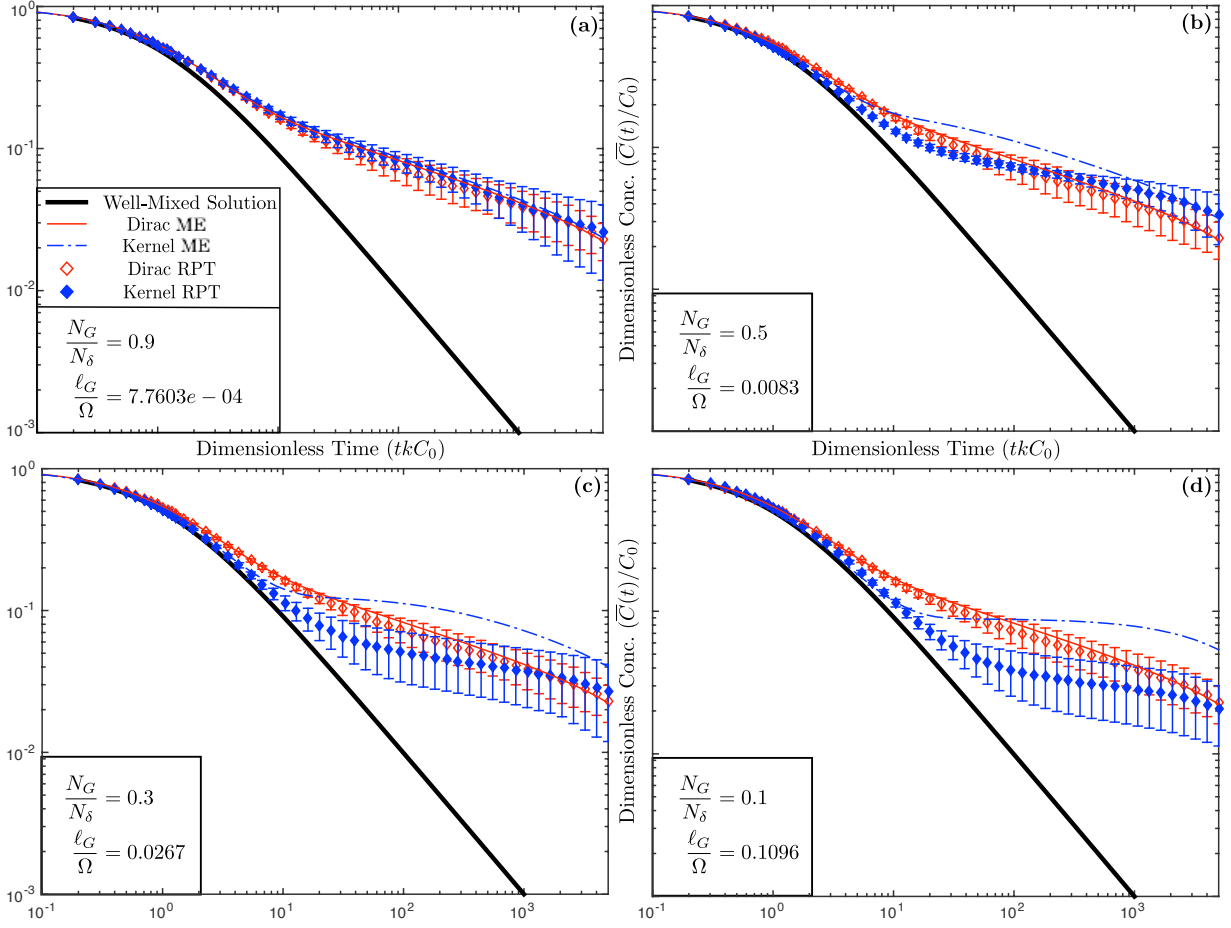


Figure 5.3: Plots of particle-tracking simulations (symbols) and moment equation solutions (curves), using least squares matching for a range of N_G/N_δ values.

decreases. For a discussion of the influence of third-order moments in a non-particle-number preserving, Dirac kernel case, see *Paster et al.* [18], though we note here that the influence of these moments appears to be significantly greater when using Gaussian kernels, due to the difference in initial conditions.

Considering Figure 5.1(b)-(d) and Figure 5.2(b)-(d), we notice a few other behaviors of interest, the effects of which increase with the ratio ℓ_G/Ω (which, in turn, increases with t^*). First, we see an increasing separation at early times between the Gaussian particle-tracking solution and the Dirac particle solution as ℓ_G/Ω increases. This phenomenon propagates through time, resulting in an overprediction of concentration at late times. Additionally,

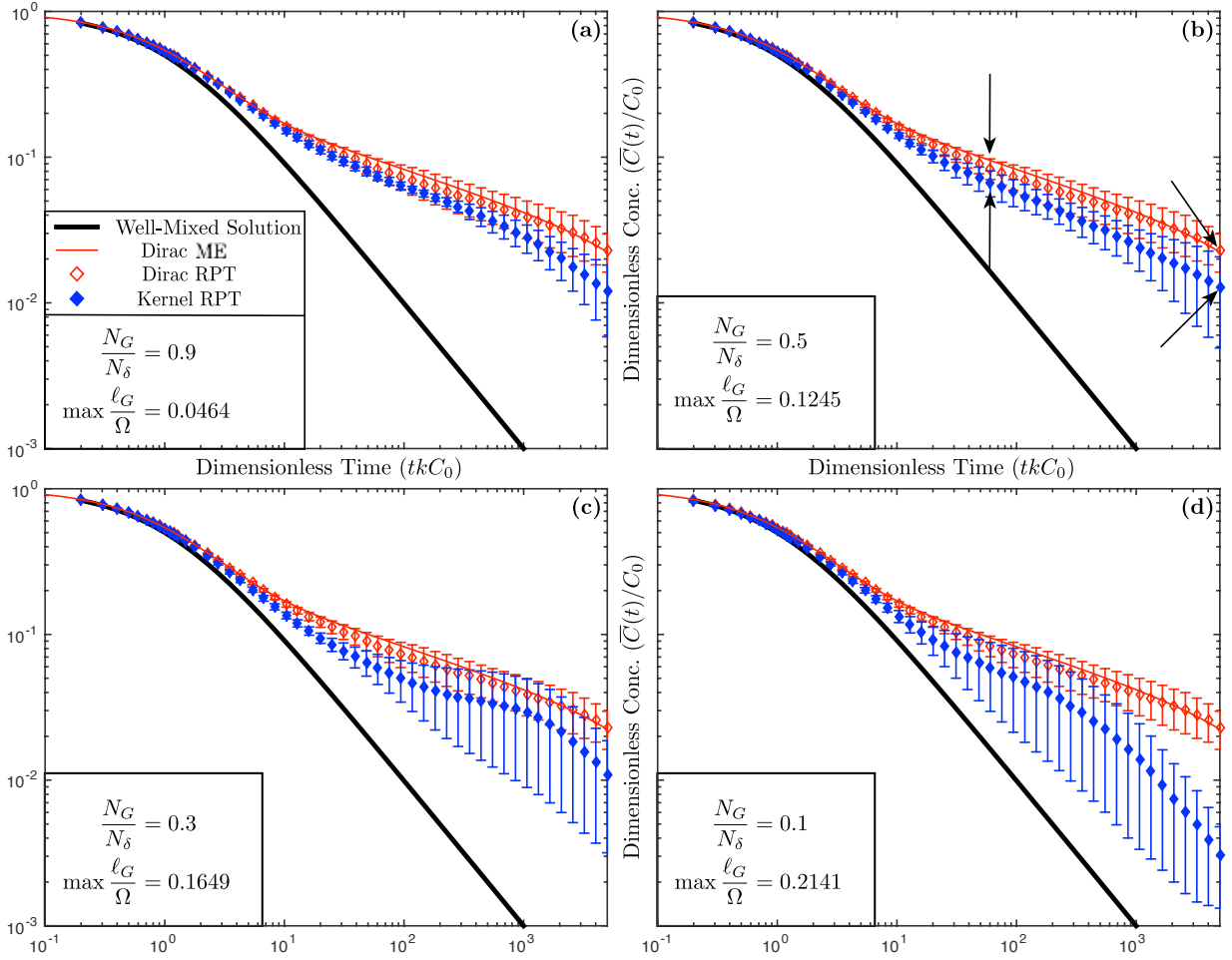


Figure 5.4: Plots of particle-tracking simulations (symbols) and moment equation solutions (curves), using variable ℓ_G matching for a range of N_G/N_δ values. Arrows in (b) correspond to the plots shown in Figure 5.8(a)-(b) and (e)-(f).

two late-time behaviors become apparent as ℓ_G/Ω increases. First, concentrations are increasingly underpredicted (which, to some extent, offsets the aforementioned overpredicting behavior, as can be seen in Figure 5.2(b), in that it shows a slightly closer match at $t^* = 1000$ than does Figure 5.2(a)). Second, as ℓ_G/Ω increases, there emerges a behavior wherein the slope of the Gaussian particle simulation becomes increasingly negative, and is seen most clearly in Figure 5.2(c) and (d). This behavior is explained in *Bolster et al.* [15] as when the particle island sizes are comparable to the domain size. These domain effects will be discussed in greater detail in Section 5.5.

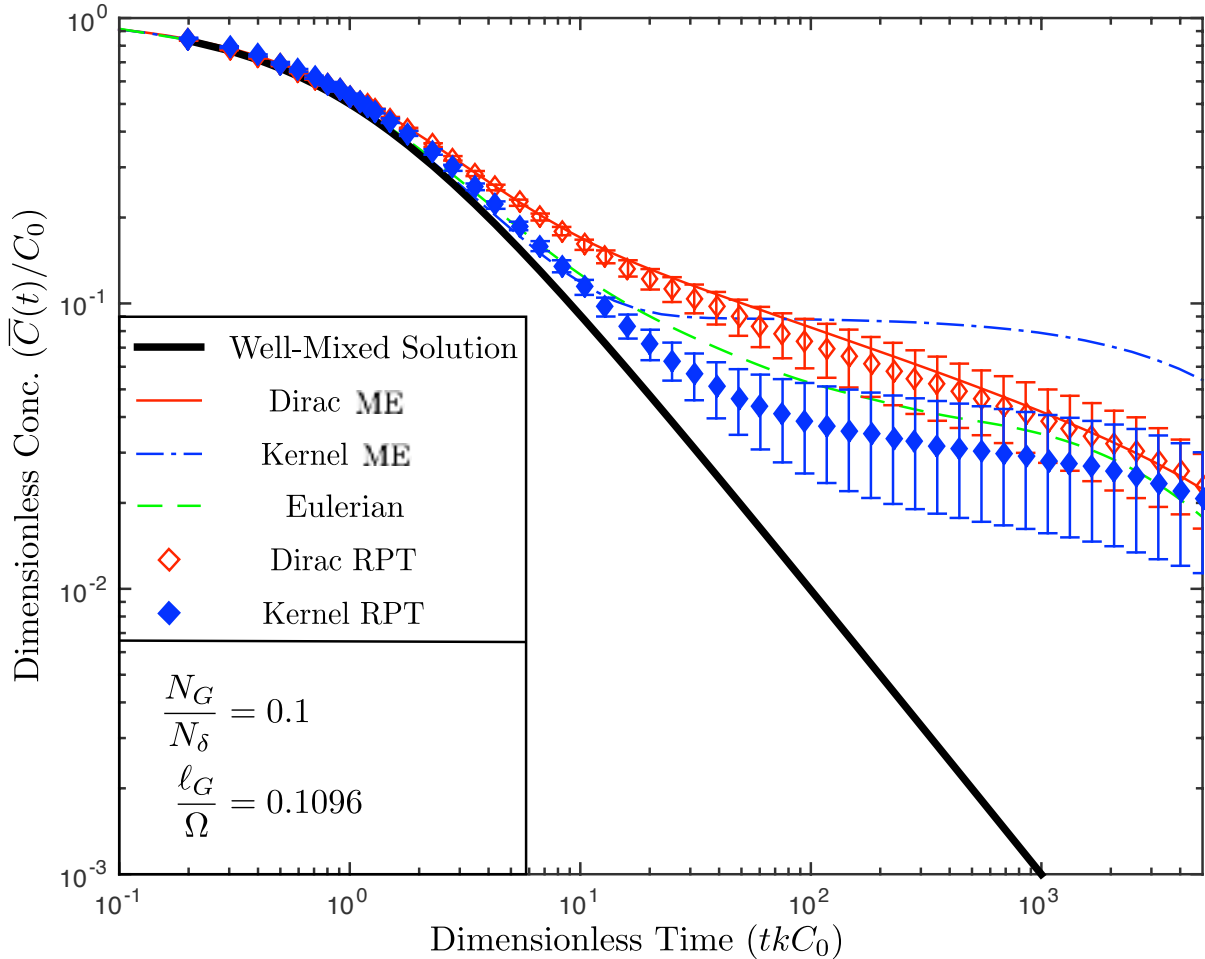


Figure 5.5: Plots of particle-tracking simulations and moment equation solutions as compared to an Eulerian finite difference solution, using the least squares matching criteria for $N_G/N_\delta = 0.1$ (corresponding to Figure 5.3(d)).

We notice that, using the specific time matching criteria, our moment equation and particle-tracking solutions show different behavior, namely the particle solutions not reliably intersecting near t^* . As an improvement, the least squares matching criteria has the potential to eliminate some of the unrecoverable errors that begin long before t^* .

5.2 Least squares matching

For these simulations, the least squares error was minimized over a set of times, T^* , with 100 logarithmically-spaced points between $t = 10^{-2}$ and 1000, according to the algorithm in Section 3.2.2. While not quite as simple to implement as the specific time matching approach,

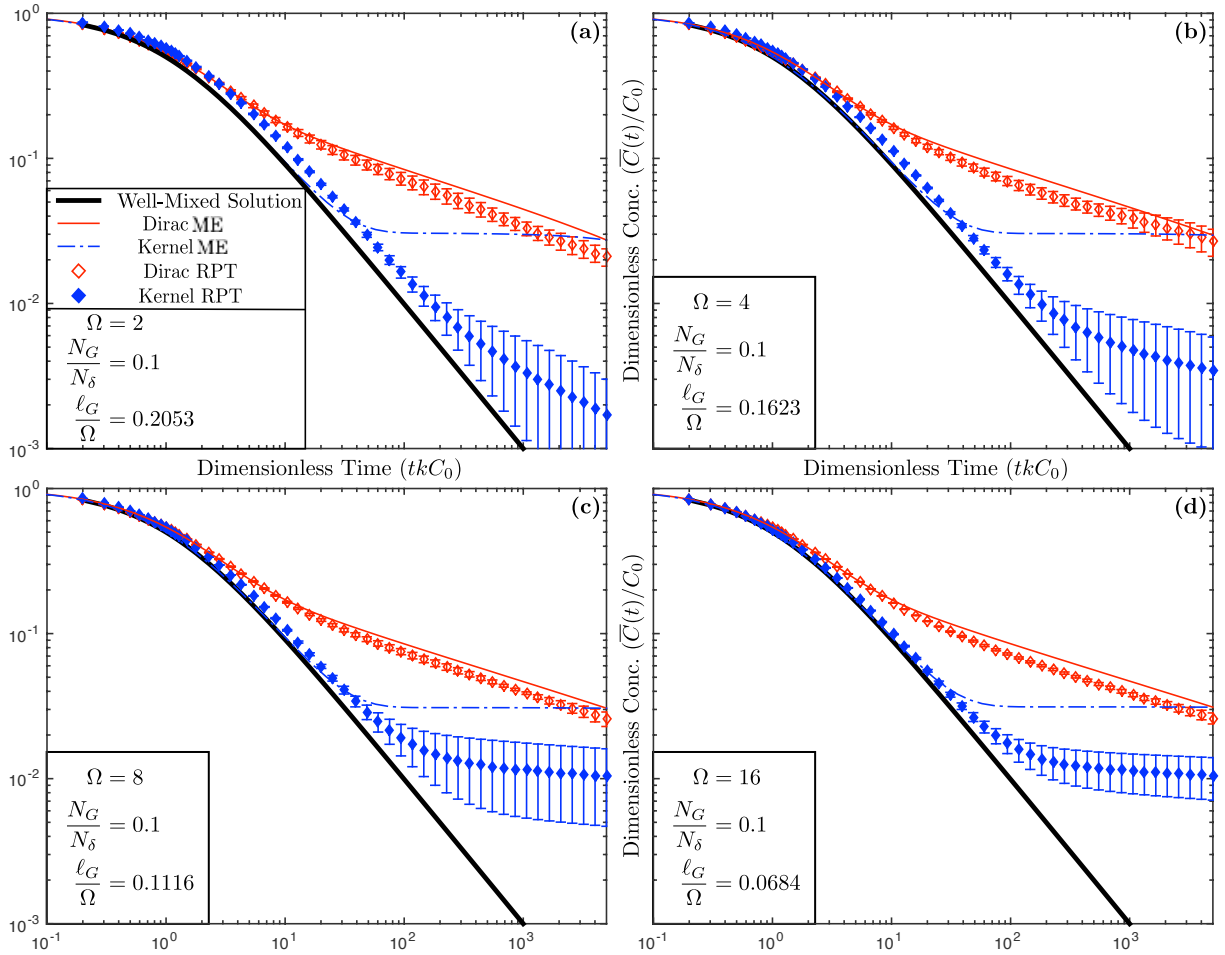


Figure 5.6: Plots of particle-tracking simulations (symbols) and moment equation solutions (curves), using specific time matching with $t^* = 1000$ ($t^*kC_0 = 5000$), $N_G/N_\delta = 0.1$ for a range of domain sizes.

we see in Figure 5.3, the least squares matching criteria shows the ability to match Dirac and Gaussian particle solutions with a high degree of fidelity. For example, the maximum error in dimensionless concentration between the particle-tracking solutions in the $N_G/N_\delta = 0.1$ case (shown in Figure 5.3(d)) is 0.0498, and final time error is 0.0023 or approximately the initial mass of five and 0.2 Gaussian particles, respectively.

Additionally, the small ℓ_G values predicted by the least squares matching (e.g., $\ell_G = 0.1096$ for $N_G/N_\delta = 0.1$, as in Figure 5.3(d), corresponds to $t^* \approx 15$) causes the above-mentioned domain effects to be an apparent non-issue for the simulated parameters. How-

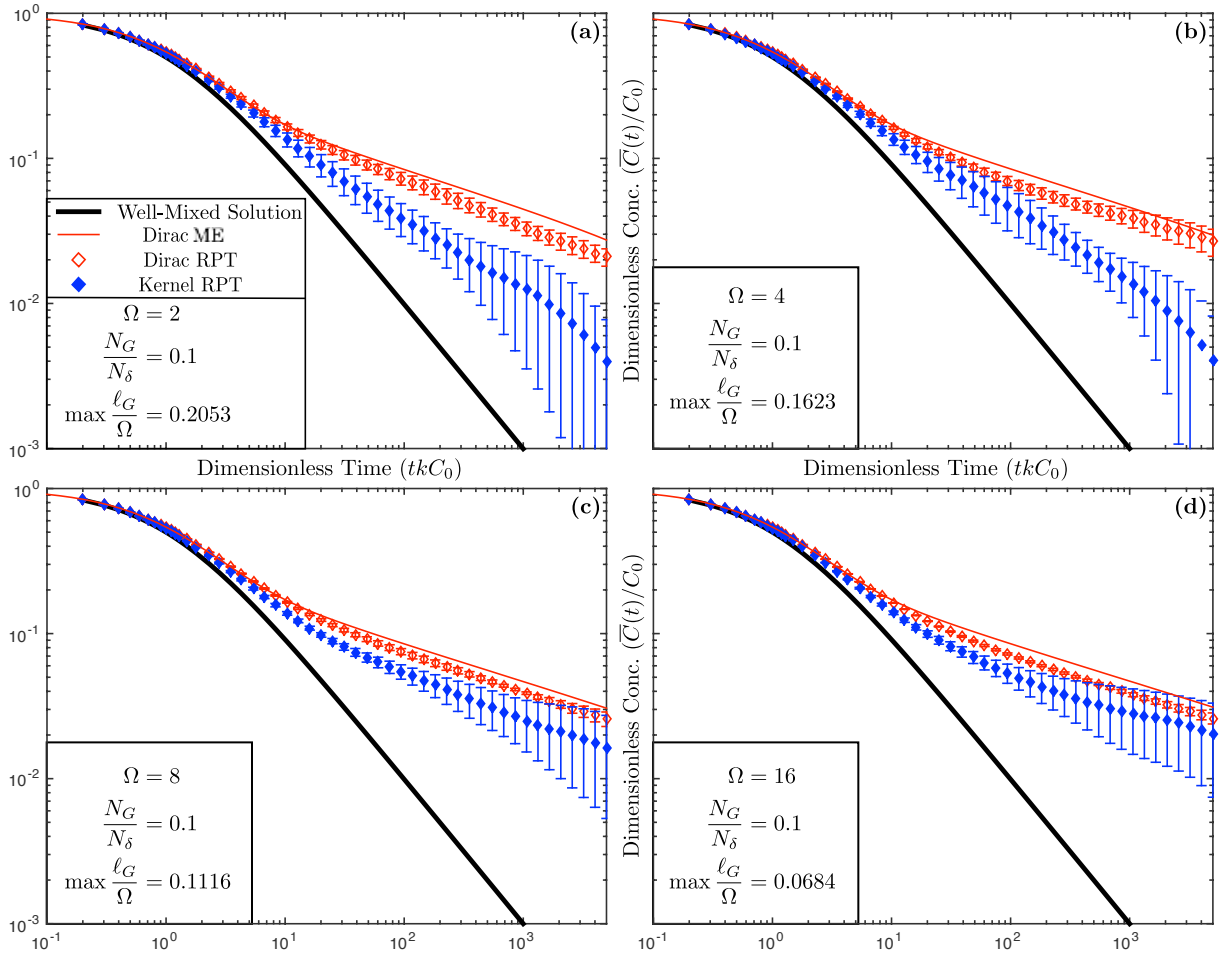


Figure 5.7: Plots of numerical simulations (symbols) and moment equation solutions (curves), using variable ℓ_G matching with $N_G/N_\delta = 0.1$ for a range of domain sizes.

ever, the effect of neglecting third-order moments is unavoidable, as is evidenced by the increasing overprediction in concentration by the moment equations as N_G/N_δ decreases. This effect is depicted most clearly in Figure 5.3(d), where the Gaussian particle solution closely matches both the particle and moment equation Dirac solutions, but the Gaussian moment equation solution differs significantly.

5.3 Variable kernel half-width matching

Another study by *Rahbaralam et al.* [19] proposed adjusting kernel size as a function of time in a simulation. We propose to treat ℓ_G as a function of time, by substituting the

simulation time, t , for t^* in (3.9). Additionally, substituting (3.9) into (3.8) and using this newly formulated cross-covariance in (3.6), we get a complicated equation for $\overline{C}_G(t)$ that may be solved numerically. The expected result prevails that $\overline{C}_\delta - \overline{C}_G \equiv 0$, as we are simply creating a condition under which g_δ and g_G are numerically equal for all chosen time steps. We admit here, and leave as an open question, that we have not generated the analytical framework to properly analyze this reformulated moment equation. Nonetheless, numerical particle-tracking simulations were conducted using this method, wherein ℓ_G is recalculated at every time step, using actual simulation time (ℓ_G is initialized using $t = \Delta t/2$), giving good overall matching to the Dirac solutions, as shown in Figure 5.4. Figure 5.4(a) and (b) show very close agreement between the Dirac and Gaussian particle simulations, while Figure 5.4(c) and (d) appear to show the effects of large ℓ_G relative to Ω .

In order to examine the capabilities of this method, simulations were conducted that attempted to decrease the domain effects (the details of which are discussed in Section 5.5). As shown in Figure 5.7, as the effect of the domain is decreased, the variable half-width kernel method converges very closely to the Dirac particle simulations (e.g., Figure 5.7(d) has a maximum error in dimensionless concentration of 0.0236, and an error of 0.0058 at final time, or approximately the mass of 2 or 0.5 Gaussian particles, respectively).

5.4 Comparison to Eulerian method

In order to further validate the kRPT model, we compare the numerical results to a classical Eulerian numerical method. In this direction, we follow a similar approach to that of *Bolster et al.* [16], in that initial concentrations are stochastically perturbed about C_0 by drawing from a uniform distribution. The method used will be a semi-implicit finite difference scheme. The linear portion of our method (diffusion) will be backward in time, central in space, and the nonlinear portion (reaction) will be backward in time, formulated as follows

$$\frac{C_i(t, x) - C_i(t - \Delta t, x)}{\Delta t} - D \frac{C_i(t, x + \Delta x) - 2C_i(t, x) + C_i(t, x - \Delta x)}{\Delta x^2} = -kC_A(t - \Delta t, x)C_B(t - \Delta t, x), \quad (5.1)$$

$$i = A, B,$$

where Δx is chosen to be $1/N_\delta$ and Δt is chosen so as to match the time steps of the particle-tracking simulations.

We compare the finite difference solution to the results of the least squares matching for $N_G/N_\delta = 0.1$ (the least squares plot shown in Figure 5.3(d)), within Figure 5.5, which shows a very close agreement between the solutions generated by both the Dirac and Gaussian particle-tracking simulations and the Eulerian finite difference simulation.

5.5 Domain effects

In each of the three methods to estimate ℓ_G , we see characteristic behaviors of finite domain effects. These include errors in concentration in the form of: early time overprediction, late time underprediction, and increasingly negative slope at late time (for a further discussion of domain effects, see *Bolster et al.* [15]). We choose two cases that seemed to suffer from the most significant domain effects, namely the specific time matching case for $N_G/N_\delta = 0.1$, $t^* = 1000$ and the variable kernel half-width case for $N_G/N_\delta = 0.1$ (shown in Figure 5.2(d) and Figure 5.4(d)).

In order to hold the Damköhler number of the systems constant as we increase the domain size from $\Omega = 1$ to $\Omega = \{2, 4, 8, 16\}$, we increase the particle number in direct proportion. This allowed us to simulate the same system (holding \widehat{Da} constant) while decreasing the values for ℓ_G/Ω . Note that since Ω appears in (3.9), this relationship is somewhat complicated, but ℓ_G increases approximately proportional to $\sqrt{\Omega}$.

As shown in Figure 5.6 and Figure 5.7, one can readily see the aforementioned domain effects decrease as ℓ_G/Ω decreases. In Figure 5.6, as the domain expands, the Gaussian particle solutions begin to converge more closely to the well-mixed analytical and Dirac particle solutions at early time. As well, in both Figure 5.6 and Figure 5.7, the sharp

turndown in slope at late time disappears as the kernels no longer “feel” effects from the boundary, and the concentration underprediction is reduced. The combination of these results leads to significantly improved agreement in both of the considered cases. While we propose no exact proof for the maximum appropriate ratio ℓ_G/Ω to minimize domain effects, our numerical results suggest that a good rule of thumb is to keep this ratio below 0.12.

5.6 Slowdown in Gaussian particle reaction speed

Examining the results of the above numerical simulations, a particular behavior becomes apparent, in that the Gaussian particle simulations tend to have an accelerated reaction rate (as compared to Dirac simulations) at early time, followed by a period during which reaction slows significantly, and finally, at late time, reaction rate increases again, and the slope of the Gaussian particle solution begins to match that of the Dirac solution. This behavior is demonstrated most clearly in Figure 5.2(b).

In order to analyze this behavior, single-realization simulations were run where position and mass were recorded for all particles as they evolve in time, and results are shown in Figure 5.8 (only particles with mass greater than 2% of the original mass of one Dirac particle are depicted). These simulations were conducted to compare the Dirac particle simulation to the Gaussian particle case of $N_G/N_\delta = 0.5$ in the two subcases of specific time matching for $t^* = 1000$ (“fixed ℓ_G ”) and variable kernel half-width matching (shown in Figure 5.2(b) and Figure 5.4(b)).

What we observe in the Dirac case is the well-documented and predictable segregation of species and the formation of “islands” due to low levels of diffusion, as shown in Figure 5.8(a) and (b), and discussed in *Toussaint and Wilczek* [23]. This segregation appears to begin around $t = 50$, with the formation of small islands (Figure 5.8(a)), and the segregation becomes quite pronounced at the final time $t = 1000$, when we are left with only two large islands (Figure 5.8(b)). However, in the fixed ℓ_G case, we see strict segregation beginning around $t = 50$, with the formation of “moats” around the islands with a width approximately $2\ell_G$ (Figure 5.8(c)). These islands and moats persist until late time (Figure 5.8(d)), when

the overall reaction is dictated by the time required for particles to migrate to the island edges.

It was this phenomenon that was the motivation for the variable ℓ_G approach discussed in Section 5.3, as a kernel that starts small and grows with time should prevent the early formation of moats (and corresponding slowdown of reaction rate), while still allowing for solution matching as time progresses and the kernel grows. We see evidence of exactly this at $t = 50$ (Figure 5.8(e)), where smaller islands have begun to form but no moats are apparent ($\ell_G(t = 50) = 0.0473$). Then, at $t = 1000$ (Figure 5.8(f)), we see a similar moat size to the fixed ℓ_G case, but with greater overall particle masses, explaining the closer fit to the Dirac solution in the variable ℓ_G case.

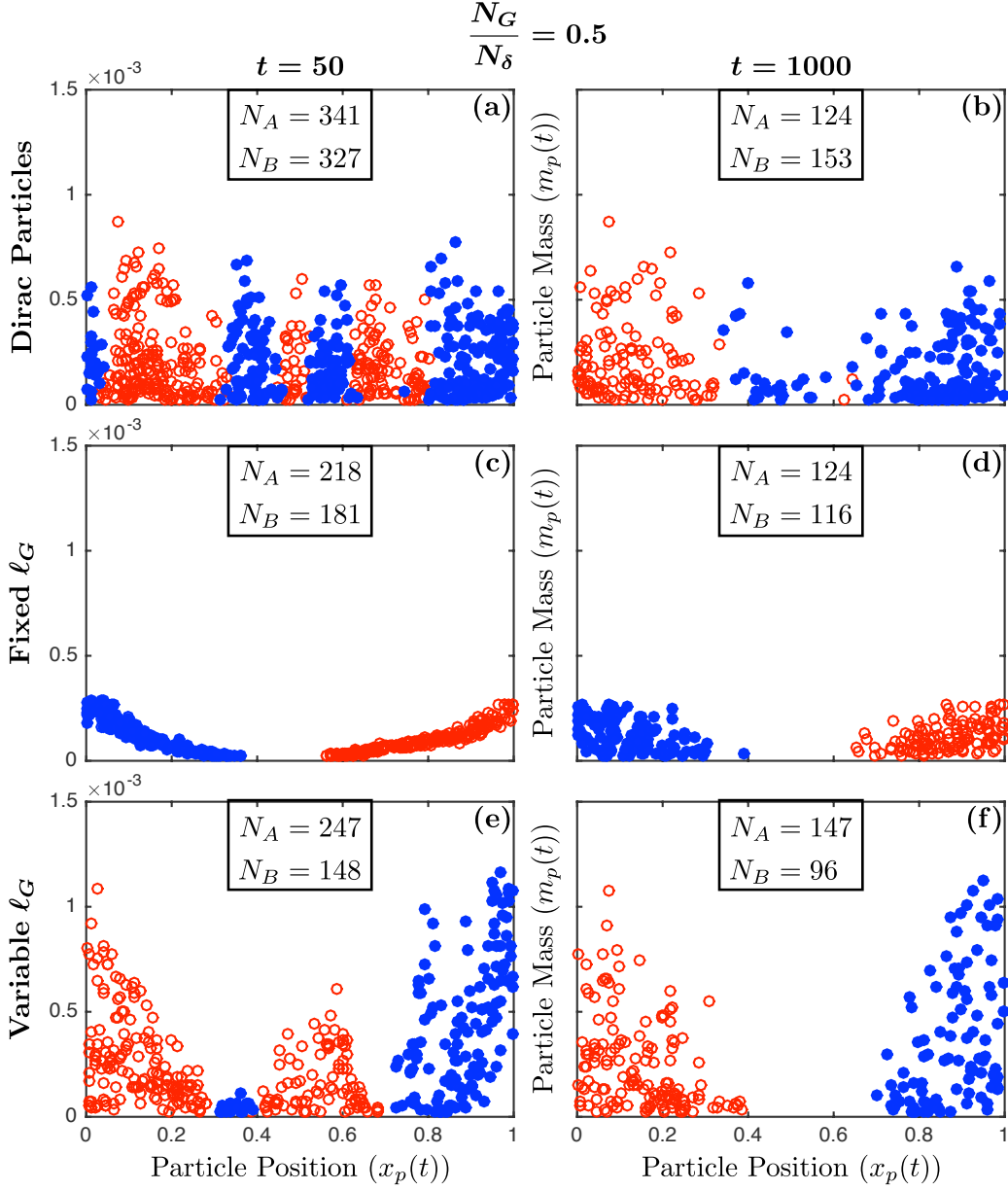


Figure 5.8: Plots of particle position/mass demonstrating moats phenomenon for Gaussian kernels (bottom two rows). Plots show $N_G/N_\delta = 0.5$ using: Dirac kernels, specific time matching (fixed ℓ_G) with $t^* = 1000$ ($t^*kC_0 = 5000$), and variable ℓ_G matching.

CHAPTER 6

CONCLUSIONS

In this text, we present a kernel-based particle-tracking method for modeling imperfectly-mixed chemical reactions in diffusive media. In particular, Gaussian kernels were chosen for computational convenience, notably the preservation of their Gaussian structure under convolution, although any kernel with similar properties could presumably be used. The primary advantage of kRPT is the ability to significantly reduce the number of particles used, as compared to a corresponding Dirac kernel-based mRPT simulation, while introducing minimal error in the solution. We first analyze the behavior of this system by deriving moment equations for a specifically-formulated system with concentration fluctuations. Using these tools, we ascertain that the error between a Dirac and Gaussian-based solution can be reduced to an arbitrary level, determined by choice of particle number and the parameters of the system. Further, we use these moment equation solutions to inform our criteria for matching the Dirac and Gaussian particle simulation solutions, essentially deducing the optimal kernel half-width from our choice of particle number by using one of three matching criteria.

The specific time matching criteria is the simplest method to implement. One need only choose the desired number of Gaussian particles, N_G , and the time at which solutions should be close, t^* , to compute the appropriate kernel size for the simulation. However, of the three methods, this one yielded the worst overall performance, as it is susceptible to error-inducing phenomena. First, the ratio of kernel half-width to domain size, ℓ_G/Ω , increases both as N_G/N_δ decreases and as t^* increases. This inevitably leads to undesirable domain effects when $\ell_G \gtrsim 0.12$ in one dimension. Additionally, the particle solutions do not intersect as reliably near t^* as the moment equation solutions do. The assumption that $|\overline{C}_\delta - \overline{C}_G| \approx 0$ on the interval $[0, t^*]$, allowing for cancellation of the exponential integral terms in (3.8), seems not to hold up in the particle case, presumably due to the increasing

effect of third-order moments as N_G/N_δ decreases.

The least squares matching criteria requires a numerical minimization of the error between moment equation solutions, but it provides a markedly better ability to minimize error in the particle simulations. This is due to the fact that, rather than assuming closeness of solutions for cancellation in order to minimize error at a single time, the algorithm minimizes the overall error in the Dirac and Gaussian moment equation solutions across a range of time values. As a result, it appears that the only source of error between our moment equation and particle-tracking simulations is the neglect of third-order moments in the moment equations.

The emergent and persistent “moat” behavior, discussed in Section 5.6, caused by the choice of a single kernel size for the duration of a simulation, led to an approach that allows the kernel half-width to grow with time. While we do not have the theoretical framework to fully analyze this method of matching, it shows strong potential as a method for matching Dirac and Gaussian solutions. One caveat, however, is that, while this variable ℓ_G method is able to minimize or eliminate domain effects at early time, it is still susceptible to domain effects at late time if $\ell_G(t)$ becomes larger than approximately 12% of the domain.

To summarize, under the circumstances considered here, the least squares matching criteria is the most effective means for using up to an order of magnitude fewer Gaussian particles and attaining similar results to the corresponding Dirac particle solution. The single caveat is to keep the ratio of ℓ_G/Ω smaller than approximately 0.12, in order to avoid error induced by domain effects.

REFERENCES CITED

- [1] I. Battiato and D. M. Tartakovsky. Applicability regimes for macroscopic models of reactive transport in porous media. *J. Contam. Hydrol.*, 120-121:18–26, 2011. doi: 10.1016/j.jconhyd.2010.05.005.
- [2] I. Battiato, D. M. Tartakovsky, A. M. Tartakovsky, and T. Scheibe. On breakdown of macroscopic models of mixing-controlled heterogeneous reactions in porous media. *Adv. Water Resour.*, 32:1664–1673, 2009. doi: 10.1016/j.advwatres.2009.08.008.
- [3] Ronnie L. Schwede, Olaf A. Cirpka, Wolfgang Nowak, and Insa Neuweiler. Impact of sampling volume on the probability density function of steady state concentration. *Water Resources Research*, 44(12):W12433, 2008. ISSN 1944-7973. doi: 10.1029/2007WR006668. URL <http://dx.doi.org/10.1029/2007WR006668>. W12433.
- [4] Gabriele Chiogna and Alberto Bellin. Analytical solution for reactive solute transport considering incomplete mixing within a reference elementary volume. *Water Resources Research*, 49(5):2589–2600, 2013. ISSN 1944-7973. doi: 10.1002/wrcr.20200. URL <http://dx.doi.org/10.1002/wrcr.20200>.
- [5] P. K. Sweby. High resolution schemes using flux limiters for hyperbolic conservation laws. *SIAM Journal on Numerical Analysis*, 21(5):995–1011, October 1984. ISSN 00361429. URL <http://www.jstor.org/stable/2156939>.
- [6] B.P. Leonard. The ultimate conservative difference scheme applied to unsteady one-dimensional advection. *Computer Methods in Applied Mechanics and Engineering*, 88(1):17–74, June 1991. ISSN 0045-7825. URL <http://www.sciencedirect.com/science/article/pii/004578259190232U>.
- [7] Randall J. LeVeque. *Finite Volume Methods for Hyperbolic Problems*. Cambridge University Press, 2002.
- [8] Olivier Bokanowski and Hasnaa Zidani. Anti-dissipative schemes for advection and application to Hamilton–Jacobi–Bellmann equations. 30(1):1–33–, 2007. ISSN 0885-7474. URL <http://dx.doi.org/10.1007/s10915-005-9017-0>.
- [9] D. T. Gillespie. Exact stochastic simulation of coupled chemical reactions. *J. Phys. Chem.*, 81(25):2340–2361, 1977.

- [10] Daniel T. Gillespie, Andreas Hellander, and Linda R. Petzold. Perspective: Stochastic algorithms for chemical kinetics. *The Journal of Chemical Physics*, 138(17):170901, 2013. doi: <http://dx.doi.org/10.1063/1.4801941>. URL <http://scitation.aip.org/content/aip/journal/jcp/138/17/10.1063/1.4801941>.
- [11] Samuel A. Isaacson. A convergent reaction-diffusion master equation. *The Journal of Chemical Physics*, 139(5):054101, 2013. doi: <http://dx.doi.org/10.1063/1.4816377>. URL <http://scitation.aip.org/content/aip/journal/jcp/139/5/10.1063/1.4816377>.
- [12] Stefan Hellander and Linda Petzold. Reaction rates for a generalized reaction-diffusion master equation. *Phys. Rev. E*, 93:013307, Jan 2016. doi: 10.1103/PhysRevE.93.013307. URL <http://link.aps.org/doi/10.1103/PhysRevE.93.013307>.
- [13] David A. Benson and Mark M. Meerschaert. Simulation of chemical reaction via particle tracking: Diffusion-limited versus thermodynamic rate-limited regimes. *Water Resour. Res.*, 44:W12201, December 2008. doi: 10.1029/2008WR007111. URL <http://dx.doi.org/10.1029/2008WR007111>.
- [14] Jeroen S. van Zon and Pieter Rein ten Wolde. Simulating biochemical networks at the particle level and in time and space: Green’s function reaction dynamics. *Phys. Rev. Lett.*, 94:128103, Apr 2005. doi: 10.1103/PhysRevLett.94.128103. URL <http://link.aps.org/doi/10.1103/PhysRevLett.94.128103>.
- [15] Diogo Bolster, Pietro de Anna, David A. Benson, and Alexandre M. Tartakovsky. Incomplete mixing and reactions with fractional dispersion. *Advances in Water Resources*, 37(0):86–93, March 2012. ISSN 0309-1708. doi: 10.1016/j.advwatres.2011.11.005. URL <http://www.sciencedirect.com/science/article/pii/S030917081100217X>.
- [16] Diogo Bolster, Amir Paster, and David A. Benson. A particle number conserving Lagrangian method for mixing-driven reactive transport. *Water Resources Research*, 52(2):1518–1527, 2016. ISSN 1944-7973. doi: 10.1002/2015WR018310. URL <http://dx.doi.org/10.1002/2015WR018310>.
- [17] David A. Benson and Diogo Bolster. Arbitrarily complex chemical reactions on particles. *Water Resources Research*, Submitted, 2016.
- [18] Amir Paster, Diogo Bolster, and David A. Benson. Connecting the dots: Semi-analytical and random walk numerical solutions of the diffusion–reaction equation with stochastic initial conditions. *Journal of Computational Physics*, 263(0):91–112, April 2014. ISSN 0021-9991. doi: 10.1016/j.jcp.2014.01.020. URL <http://www.sciencedirect.com/science/article/pii/S0021999114000473>.

- [19] Maryam Rahbaralam, Daniel Fernández-García, and Xavier Sanchez-Vila. Do we really need a large number of particles to simulate bimolecular reactive transport with random walk methods? A kernel density estimation approach. *Journal of Computational Physics*, 303:95 – 104, 2015. ISSN 0021-9991. doi: <http://dx.doi.org/10.1016/j.jcp.2015.09.030>. URL <http://www.sciencedirect.com/science/article/pii/S0021999115006233>.
- [20] K Kang and S Redner. Scaling approach for the kinetics of recombination processes. *Physical Review Letters*, 52:955–958, 1984.
- [21] A. A. Ovchinnikov and Y. B. Zeldovich. Role of density fluctuations in bimolecular reaction kinetics. *Chem. Phys.*, 28:215–218, 1978.
- [22] K. Kang and S. Redner. Fluctuation effects in Smoluchowski reaction-kinetics. *Physical Review A*, 30(5):2833–2836, 1984. doi: 10.1103/PhysRevA.30.2833.
- [23] D. Toussaint and F. Wilczek. Particle–antiparticle annihilation in diffusive motion. *J. Chem. Phys.*, 78(5):2642–2647, 1983.
- [24] A.M. Tartakovsky, P. de Anna, T Le Borgne, A Balter, and D Bolster. Effect of spatial concentration fluctuations on effective kinetics in diffusion-reaction systems,. *Water Resources Research*, 48:W02526, 2012.
- [25] A. Paster, D. Bolster, and D. A. Benson. Particle tracking and the diffusion-reaction equation. *Water Resour. Res.*, 49:1–6, 2013. ISSN 1944-7973. doi: 10.1029/2012WR012444.

APPENDIX A

INITIAL COVARIANCE RELATIONS FOR THE PARTICLE-TRACKING METHOD

Following a similar approach to *Paster et al.* [18], we wish to derive representations for initial auto- and cross-covariance in concentration fluctuations for the particle-tracking model. It is assumed that initial particle positions are independent and identically distributed and determined by drawing from a uniform probability distribution. Throughout, we assume Ω is chosen to be sufficiently large, so as to exclude boundary effects caused by utilizing a finite computational domain (we investigate the effects of such finite domains numerically in Section 5.5).

The concentrations composed of particles will be of the form

$$\begin{aligned} C_i(t, x) &= \sum_{k=1}^N \int_{\Omega} m_p \phi_i(x - z) \delta(z - x_k) dz, \quad i = A, B, \\ &= m_p \sum_{k=1}^N \phi_i(x - x_k), \end{aligned} \tag{A.1}$$

where $x_k(t)$ is the position of the k^{th} of N particles, m_p is the initial mass of a single particle (particle number and initial mass are assumed to be equal for A and B particles, for simplicity in calculations), and Ω is a d -dimensional domain. The kernel ϕ_i is defined to be symmetric ($\phi_i(x - z) = \phi_i(z - x)$), have units L^{-d} , and for Ω suitably large, to integrate approximately to unity ($\int_{\Omega} \phi_i(x) dx \approx 1$). For simplification in computation, we assume this approximation to be close enough so as to consider this integral equal to 1.

Thus, we may represent average concentration

$$\begin{aligned} \bar{C}_i(t) &= \mathbb{E} [C_i(t, x)] = \frac{1}{\Omega} \int_{\Omega} C_i(t, x) dx \\ &= \frac{Nm_p}{\Omega}. \end{aligned} \tag{A.2}$$

Using the relation in (2.3), initial autocovariance may be represented by $\overline{C'_i(0, x)C'_i(0, y)} = \overline{C_i(0, x)C_i(0, y)} - \bar{C}_i(0)^2$, yielding

$$\overline{C'_i(x)C'_i(y)} = m_p^2 \int_{\Omega^N} \cdots \int_{\Omega^N} \left[\sum_{k=1}^N \sum_{l=1}^N \phi_i(x - x_k) \phi_i(y - x_l) F(x_1, \dots, x_N) \right] dx_1 \dots dx_N - \left(\frac{Nm_p}{\Omega} \right)^2, \quad (\text{A.3})$$

where $F(x_1, \dots, x_N)$ is the joint pdf for the randomly distributed particles. Since the particle positions are independent of each other, $F(x_1, \dots, x_N) = F(x_1) \dots F(x_N) = \Omega^{-N}$, so the first term in (A.3) becomes

$$m_p^2 \int_{\Omega^N} \cdots \int_{\Omega^N} \left[\sum_{k=1}^N \sum_{l=1}^N \phi_i(x - x_k) \phi_i(y - x_l) \frac{1}{\Omega^N} \right] dx_1 \dots dx_N. \quad (\text{A.4})$$

Now, first considering the cases above where $k \neq l$, we have

$$\begin{aligned} m_p^2 \sum_{\substack{k=1 \\ k \neq l}}^N \sum_{\substack{l=1 \\ l \neq k}}^N \left[\int_{\Omega^N} \cdots \int_{\Omega^N} \left[\phi_i(x - x_k) \phi_i(y - x_l) \frac{1}{\Omega^N} \right] dx_1 \dots dx_N \right] \\ = \frac{N(N-1)m_p^2}{\Omega^2} \int_{\Omega} \phi_i(x - x_k) dx_k \int_{\Omega} \phi_i(y - x_l) dx_l \\ = \frac{N(N-1)m_p^2}{\Omega^2}, \end{aligned} \quad (\text{A.5})$$

and when $k = l$

$$\frac{Nm_p^2}{\Omega} \int_{\Omega} \phi_i(x - x_k) \phi_i(y - x_k) dx_k = \frac{Nm_p^2}{\Omega} (\phi_i \star \phi_i)(x - y), \quad (\text{A.6})$$

where \star denotes convolution. Thus, we have a general representation for initial autocovariance

$$\overline{C'_i(x)C'_i(y)} = \frac{Nm_p^2}{\Omega} \left[(\phi_i \star \phi_i)(x - y) - \frac{1}{\Omega} \right]. \quad (\text{A.7})$$

For the specific Dirac delta and Gaussian kernel choices

$$\begin{aligned} \phi_{\delta}(x - y) &= \delta(x - y), \\ \phi_G(x - y) &= \frac{1}{(2\pi\ell_G^2)^{d/2}} e^{-\frac{|x-y|^2}{2\ell_G^2}}, \end{aligned} \quad (\text{A.8})$$

we have the following initial autocovariance structures

$$\begin{aligned}
\widehat{f}_\delta(x-y) &= \frac{N_\delta m_\delta^2}{\Omega} \left[\delta(x-y) - \frac{1}{\Omega} \right] \\
&= C_0 m_\delta \left[\delta(x-y) - \frac{1}{\Omega} \right], \\
\widehat{f}_G(x-y) &= \frac{N_G m_G^2}{\Omega} \left[\frac{1}{(4\pi\ell_G^2)^{d/2}} e^{-\frac{|x-y|^2}{4\ell_G^2}} - \frac{1}{\Omega} \right] \\
&= C_0 m_G \left[\frac{1}{(4\pi\ell_G^2)^{d/2}} e^{-\frac{|x-y|^2}{4\ell_G^2}} - \frac{1}{\Omega} \right].
\end{aligned} \tag{A.9}$$

Next we calculate the initial cross-covariance, which is assumed to be reflexive as to particle type, so

$$\begin{aligned}
\overline{C'_A(0,x)C'_B(0,y)} &= \overline{C'_B(0,x)C'_A(0,y)} \\
&= \overline{C_A(0,x)C_B(0,y)} - \overline{C_A(0)}\overline{C_B(0)}.
\end{aligned} \tag{A.10}$$

Considering the first term in (A.10)

$$\overline{C_A(x)C_B(y)} = \frac{m_p^2}{\Omega^{2N}} \int \cdots \int_{\Omega^{2N}} \sum_{k=1}^N \sum_{l=1}^N \phi_A(x-x_k)\phi_B(y-y_l) dx_1, \dots, dx_N, dy_1, \dots, dy_N. \tag{A.11}$$

In contrast to the autocovariance calculations, x_k is never equal to y_l , since every A and B particle combination has probability zero of occupying the same position. As a result, we have

$$\frac{N^2 m_p^2}{\Omega^2} \int_{\Omega} \int_{\Omega} \phi_A(x-x_k)\phi_B(y-y_l) dx_k dy_l = \frac{N^2 m_p^2}{\Omega^2}. \tag{A.12}$$

Now, considering the second term in (A.10), we find

$$\overline{C_A} \overline{C_B} = \frac{N^2 m_p^2}{\Omega^2}. \tag{A.13}$$

As such, it is apparent that our initial cross-covariance is identically equal to zero.

APPENDIX B
ESTIMATES FOR ERROR PROPAGATION

In order to justify the error estimates of Chapter 4, we first show some properties of the mean concentration equations. Recall that, regardless of the choice of correlation structure, the mean concentration \bar{C} satisfies

$$\left. \begin{aligned} \frac{d\bar{C}}{dt} &= -k [\bar{C}^2 + g(t)] \\ \bar{C}(0) &= C_0 \end{aligned} \right\}, \quad (\text{B.1})$$

where

$$g(t) = \frac{1}{2(8\pi Dt)^{d/2}} \int f(0, z, x) e^{-\frac{|x-z|^2}{8Dt}} dz \left[-1 + \exp \left(-4k \int_0^t \bar{C}(\tau) d\tau \right) \right]. \quad (\text{B.2})$$

Since $g(t) = 0$ when $\bar{C} \equiv 0$, we see that $\bar{C} \equiv 0$ is an equilibrium point of the differential equation. Thus, because we take $C_0 > 0$, it follows that $\bar{C}(t) > 0$ for every $t \geq 0$ by uniqueness of solutions to (B.1). With this, we see that $g(t) < 0$ for every $t > 0$ because $\frac{1}{(8\pi Dt)^{d/2}} \int f(0, z, x) e^{-\frac{|x-z|^2}{8Dt}} dz \geq 0$ for sufficiently large Ω and the last term in (B.2) is negative. Therefore, using the negativity of g , we find from (B.1)

$$\frac{d\bar{C}}{dt} > -k\bar{C}^2,$$

for all $t > 0$. Because $\bar{C}(t) > 0$, we may use the separable nature of this inequality to find

$$\frac{d}{dt} (\bar{C}(t)^{-1}) < k,$$

which, upon integrating, finally implies for every $t > 0$

$$\bar{C}(t) > \frac{C_0}{1 + kC_0t}.$$

Since both \overline{C}_δ and \overline{C}_G satisfy a differential equation of this type, each must satisfy the same lower bound, namely

$$\overline{C}_p(t) > \frac{C_0}{1 + kC_0t}, \quad (\text{B.3})$$

for $p = \delta, G$. This result merely displays the influence of the cross-covariance function so that the negative values of g_p arising from spatial fluctuations cause the mean concentration to decrease at a slower rate than the well-mixed solution.

The above inequality further establishes an upper bound of growth on the exponential that appears in the g_p terms. In particular, using (B.3) we find

$$-4k \int_0^t \overline{C}_p(\tau) d\tau < -4k \int_0^t \frac{C_0}{1 + kC_0\tau} d\tau = -4 \ln(1 + kC_0t),$$

and thus

$$\exp\left(-4k \int_0^t \overline{C}_p(\tau) d\tau\right) < (1 + kC_0t)^{-4}. \quad (\text{B.4})$$

Finally, we consider the difference in forcing terms generated by different initial cross-covariances, namely $|g_\delta(t) - g_G(t)|$ where each individual cross-covariance $g_p(t)$ is defined by (2.12). Subtracting the equations, we find

$$\begin{aligned} |g_\delta(t) - g_G(t)| &= \left| \psi_\delta(t) \left(-1 + e^{-4k \int_0^t \overline{C}_\delta(\tau) d\tau}\right) - \psi_G(t) \left(-1 + e^{-4k \int_0^t \overline{C}_G(\tau) d\tau}\right) \right| \\ &\leq I + II, \end{aligned}$$

where

$$I := \left(1 - e^{-4k \int_0^t \overline{C}_G(\tau) d\tau}\right) |\psi_\delta(t) - \psi_G(t)|,$$

and

$$II := |\psi_\delta(t)| \left| e^{-4k \int_0^t \overline{C}_\delta(\tau) d\tau} - e^{-4k \int_0^t \overline{C}_G(\tau) d\tau} \right|.$$

We note that near $t = 0$ each these terms tend to zero, and this can be verified by a simple use of L'Hospital's Rule. Thus, there is no singularity at $t = 0$ and we will concentrate on

bounding these terms for t suitably large. Since the exponential in I is nonnegative, we find

$$\begin{aligned} I &\leq |\psi_\delta(t) - \psi_G(t)| \\ &\leq \frac{1}{2}C_0 \left(\frac{1}{\Omega} |m_\delta - m_G| + \left| \frac{m_\delta}{(8\pi Dt)^{d/2}} - \frac{m_G}{(4\pi\ell_G^2 + 8\pi Dt)^{d/2}} \right| \right) \\ &=: I_A + I_B. \end{aligned}$$

Now, because $C_0\Omega = m_p N_p$ for $p = \delta, G$ the first term is exactly

$$I_A = \frac{1}{2}C_0^2 \left(\frac{1}{N_G} - \frac{1}{N_\delta} \right) = \frac{1}{2}C_0^2\Delta.$$

Using the Mean Value Theorem on the function $h(x) = (x + 8\pi Dt)^{-d/2}$ so that

$$|h(0) - h(4\pi\ell_G^2)| \leq 4\pi\ell_G^2 \max_{x \in [0, 4\pi\ell_G^2]} |h'(x)| \leq \frac{2\pi d\ell_G^2}{(8\pi Dt)^{1+d/2}},$$

the second term satisfies

$$\begin{aligned} I_B &\leq \frac{1}{2}C_0 \left(\frac{|m_\delta - m_G|}{(8\pi Dt)^{d/2}} + m_G \left| \frac{1}{(8\pi Dt)^{d/2}} - \frac{1}{(4\pi\ell_G^2 + 8\pi Dt)^{d/2}} \right| \right) \\ &\leq \frac{C_0^2\Delta}{2\Omega(8\pi Dt)^{d/2}} + \frac{\pi d C_0 \ell_G^2 m_G}{(8\pi Dt)^{1+d/2}}. \end{aligned}$$

To estimate II , we use (4.3) to find

$$|\psi_\delta(t)| \leq \frac{1}{2\Omega} C_0 m_\delta,$$

for $t \geq \frac{\Omega^{2/d}}{8\pi D}$. Then, using (B.4) it follows that

$$II \leq \frac{C_0 m_\delta}{2\Omega} (1 + kC_0 t)^{-4}.$$

Recomposing these expressions within the inequality for the g terms, we have

$$|g_\delta(t) - g_G(t)| \leq \frac{1}{2}C_0^2\Delta + \frac{C_0^2\Delta}{2\Omega(8\pi Dt)^{d/2}} + \frac{\pi dC_0\ell_G^2 m_G}{(8\pi Dt)^{1+d/2}} + \frac{C_0 m_\delta}{2\Omega}(1 + kC_0t)^{-4}.$$

Finally, for simplicity we will assume within this analysis that $8\pi D > kC_0$ so that for $t \geq \frac{1}{8\pi D - kC_0}$, we have the inequality

$$\frac{1}{8\pi Dt} \leq \frac{1}{1 + kC_0t},$$

and thus

$$|g_\delta(t) - g_G(t)| \leq \frac{1}{2}C_0^2\Delta + \frac{C_0^2\Delta}{2\Omega(1 + kC_0t)^{d/2}} + \frac{\pi dC_0\ell_G^2 m_G}{(1 + kC_0t)^{1+d/2}} + \frac{C_0 m_\delta}{2\Omega(1 + kC_0t)^4}. \quad (\text{B.5})$$

It should be noted that a nearly identical analysis can be conducted when $8\pi D \leq kC_0$, which merely results in replacing the $(1 + kC_0t)$ terms in (B.5) with $8\pi Dt$, which is also $\mathcal{O}(t)$ as $t \rightarrow \infty$. As can be seen in Chapter 4, this will yield identical conclusions and estimates on the error incurred by using the kernel-based method rather than the Dirac-based RPT method.